

Global variability of high nutrient low chlorophyll regions using neural networks and wavelet coherence analysis.

Gotzon Basterretxea¹, Joan S. Font-Muñoz¹, Ismael Hernández-Carrasco², Sergio A. Sañudo-Wilhelmy³

¹ Department of Marine Ecology, Instituto Mediterráneo de Estudios Avanzados, IMEDEA (UIB-CSIC), Miquel Marqués 21, 07190 Esporles, Illes Balears, Spain.

² Department of Oceanography and Global Change, Instituto Mediterráneo de Estudios Avanzados, IMEDEA (UIB-CSIC), Miquel Marqués 21, 07190 Esporles, Illes Balears, Spain.

³ Department of Biological Sciences and Department of Earth Sciences, University of Southern California, Marine Biology and Biological Oceanography, Los Angeles, California 90089-0371, United States.

Correspondence to: Gotzon Basterretxea (gotzon@imedea.uib-csic.es)

Abstract. We examine 20 years of monthly global ocean color data and modeling outputs of nutrients using self-organizing map (SOM) analysis to identify characteristic spatial and temporal patterns of High Nutrient Low Chlorophyll (HNLC) regions and their association with different climate modes. The global nitrate to chlorophyll ratio threshold of $\text{NO}_3:\text{Chl} > 17$ ($\text{mmol NO}_3/\text{mg Chl}$) is estimated to be a good indicator of the distribution limit of this unproductive biome that, on average, covers $92 \times 10^6 \text{ km}^2$ (~25% of the ocean). The trends in satellite-derived surface chlorophyll (0.6 ± 0.4 to $2 \pm 0.4\% \text{ yr}^{-1}$) suggest that HNLC regions in polar and subpolar areas have experienced an increase in phytoplankton biomass over the last decades but much of this variation is produced by a climate-driven transition in 2009-2010. Indeed, since 2010, the extent of the HNLC zones has decreased at the poles (up to 8%) and slightly increased at the equator (<0.5%). Our study finds that chlorophyll variations in HNLC regions respond to major climate variability signals Chlorophyll variations in HNLC regions respond to major climate variability signals such as El Niño Southern Oscillation (ENSO) and Meridional Overturning Circulation (MOC) at both short (2-4 years) and long (decadal) timescales. These results suggest global coupling in the functioning of distant biogeochemical regions.

1 Introduction

High nutrient low chlorophyll (HNLC) areas are ocean regions where primary production should be potentially high but phytoplankton biomass remains relatively low and constant despite the perennial nutrient availability for growth (Martin and Fitzwater, 1988; Chisholm and Morel, 1991). They are interesting regions because they challenge the accepted paradigm of a positive relation between macronutrient concentrations and phytoplankton biomass in open waters but, most importantly, because they represent an important fraction of the global ocean carbon budgets and, therefore, their extent influences the potential withdrawal of atmospheric CO_2 to the deep ocean (Martin et al., 1990; de Baar et

34 al., 1995; Boyd et al., 2005). It is estimated that HNLC biomes roughly cover between 20 and 30% of the
35 world's oceans (Pitchford and Brintley, 1999; Tyrrel et al., 2005) comprising three major ocean areas; the
36 Subarctic North Pacific (SNP), the Eastern Equatorial Pacific (EEP) and most of the Southern Ocean (SO)
37 (Martin, 1990; Coale et al., 1996; Parekh et al., 2005).

38 Because nitrogen is the mineral nutrient needed in greatest abundance by phytoplankton and owing to its
39 generalized depletion in surface waters over much of the oceans, it is considered a key limiting nutrient
40 for ocean production. In HNLC regions, where nitrogen is in excess, other non-exclusive factors such as
41 rapid top-down control by zooplankton grazing, low irradiance, limitations by silicic acid availability,
42 and/or iron (Fe) limitation, have been hypothesized to explain the persistently low chlorophyll (Chl).
43 While these factors may contribute in different degrees to the observed low Chl and determine the
44 phytoplankton dynamics in HNLC regions (see Chavez et al., 1991; Cullen, 1995; Coale et al., 1996;
45 Dugdale and Wilkerson, 1998; Landry et al., 2011), it is generally acknowledged that Fe availability is
46 central to the productivity of HNLC regions (Boyd et al., 2007). All HNLC regions share a chronic Fe-
47 depletion in surface waters and experimental results show highly positive productivity responses to Fe
48 addition (Martin et al., 1994; Boyd et al., 2000, 2004; Tsuda et al., 2003; Coale et al., 2004). Indeed, iron
49 is required in largest amounts than any of the trace metals for several metabolic processes, and not
50 surprisingly, it has been considered the ultimate limiting nutrient (Moore and Doney, 2007). This has led
51 to propose a conceptual model of phytoplankton nutrient limitation in the modern ocean based on two
52 functioning regimes: one in which the supply of nutrients is relatively slow and nitrogen availability limits
53 productivity, and a complementary regime, with enhanced nutrient supply, where Fe often limits
54 productivity (Moore et al., 2013).

55 Iron limitation influences the uptake of nitrogen thereby explaining the unused nitrate concentrations in
56 HNLC regions. Indeed, it has been proposed that a delicate balance between nitrogen and Fe availability
57 modulates phytoplankton growth and that co-limitation is rather ubiquitous in the sea (Bryant, 2003;
58 Browning et al., 2017). Other elements and compounds such as B-vitamins, which are also scarce in Fe-
59 limited areas, can also be co-limiting factors for phytoplankton growth in these regions (e.g. Koch et al.,
60 2011; Bertrand et al., 2012). For example, it has been experimentally shown that the addition of Fe and
61 B12 to Antarctic phytoplankton assemblages can synergistically increase phytoplankton growth (Bertrand
62 et al., 2011; Cohen et al., 2017).

63 Despite their relevance for global ocean productivity and carbon fluxes, HNLC regions remain loosely
64 defined and knowledge of their temporal and spatial variability and trends is limited. Moreover, their
65 response in a global warming scenario is uncertain. Only general aspects such as expected shifts in
66 phytoplankton community composition or changes in Fe-cycling rates have been addressed to date (Fu et
67 al., 2016; Lauderdale et al., 2020). The original description of HNLC systems by Minas et al. (1986)

68 referred to a slowly growing phytoplankton standing stock despite the presence of high nutrient
69 concentrations. However, there are no rigid criteria accurately defining the functioning of these
70 ecosystems. Several ecosystem characteristics such as species composition, biological structure, carbon
71 utilization pathways, and response to climate change also differ between the HNLC and other ecosystems,
72 reflecting differences in the limiting factor (e.g. Falkowski et al., 1998; Ono et al., 2008).

73 Of particular interest are the aspects related to the reduced variability and high permanence (i.e. temporal
74 persistence) typically characterizing large HNLC regions. These features are distinctive from those of
75 highly variable systems, which may temporarily present HNLC conditions. For example, some light-
76 limited regions in high latitudes may present low productivity and enhanced nutrients during winter but
77 it responds to a transient situation that does not correspond to the generally accepted HNLC paradigm.
78 Similarly, high nutrients and low Chl have been observed at the end of the spring bloom in some
79 productive systems (Nielsdóttir et al., 2009) and some areas located in coastal upwelling regions
80 (Hutchins et al., 1998, 2002; Firme et al., 2003; Eldridge et al., 2004). While complying with the necessary
81 conditions of high nutrient and low Chl, it is uncertain whether these ephemeral systems share structural
82 and functioning similitudes with the large HNLC regions.

83 At a time when understanding biogeochemical responses to large-scale forcings, including climate
84 change, has become a scientific priority, it seems appropriate to revisit some concepts of the functioning
85 of HNLC regions. Their extent and variability are indicative of the dynamic changes in the bidirectional
86 interrelationships of phytoplankton with the environment and with other organisms at large scales. Most
87 of the information on the long-term variations of HNLC regions is depicted from global studies suggesting
88 that their productivity is declining and that they experience prominent interannual to decadal fluctuations
89 superimposed on these long-term trends (i.e. Boyce et al., 2010). Available evidence suggests that some
90 HNLC regions may be decreasing in size as a result of increased ocean stratification (Ono et al., 2008).
91 More recently, Yasunaka et al., (2016), determined that surface trends of phosphate and silicate in the
92 North Pacific are associated with the shoaling of the mixed layer, reporting that surface nutrient
93 concentration was correlated with the North Pacific Gyre Oscillation (NPGO). Some studies have shown
94 that oligotrophic areas in the northern hemisphere are expanding between 0.8 and 4% per year, with a
95 faster increase in winter months (Polovina et al., 2008). However, with some exceptions (e.g. Radenac
96 et al., 2012; Yasunaka et al., 2014), specific long-term studies on HNLC regions are scarce and knowledge
97 on their variability in the global ocean scale and their response to climate change remain uncertain.

98 The objective of the present study is to provide a quantitative assessment of the large-scale patterns of
99 variability of the three major HNLC regions (SNP, EEP, and SO) and their relationship with the main
00 modes of climate variability. Systematically determining the boundaries of these HNLC regions has
01 remained elusive since it requires coherent information on nutrients and Chl fields. The present study is

02 based on the analysis of 20-year time series of monthly global ocean color data and nutrient concentrations
03 from a biogeochemical model using machine learning techniques and wavelets analysis. First, based on
04 the statistical analysis of global NO₃:Chl ratios, we determine a robust quantitative criterion to objectively
05 define HNLC regions. Then we characterize the temporal variability patterns of HNLC regions based on
06 their NO₃ and Chl concentrations by using the Self-Organizing Map (SOM) technique. We use the herein-
07 established statistical criterion to assess the spatial variations of HNLC regions over the study period
08 unveiled from the SOM analysis in the spatial domain of NO₃:Chl ratios. Finally, through a combined
09 SOM-wavelet coherence analysis (WCA), we quantify the spectral power and the dynamic relationship
10 between the observed Chl variability and two main global-scale forcings; El Niño Southern Oscillation
11 (ENSO); and Meridional Overturning Circulation (MOC). We show that the combination of WCA with
12 SOM-derived characteristic time-series is an especially suitable tool for the analysis of driver-response
13 relationships in the ocean.

14 **2 Materials and Methods**

15 *2.1 Ocean color data*

16 We employ 20 years of monthly global composites of satellite Chl Level-3 products, derived from
17 merging SeaWiFS, MERIS, MODIS AQUA, and VIIRS sensors using a GSM algorithm (Maritorena and
18 Siegel, 2005), obtained from GlobColour data set (www.globcolour.info). The chlorophyll product is
19 spatially gridded, and the weighted average of the different merged Level-2 products is then calculated.
20 The composite consists of a rectangular regular map product in degrees with a spatial resolution of 0.25°
21 (i.e. around 28 km at the equator that varies with the latitude) and covers the period from January 1998
22 to December 2017. We excluded results in the Arctic Ocean and the coastal Southern Ocean due to the
23 interference of ice cover and prolonged gaps in the data. A total of 654395 pixels were considered in the
24 analysis. We are aware that the consistency of merged multi-mission ocean color satellite series may
25 suffer from some limitations influencing long trend analysis (Mèlin et al., 2017). However, no significant
26 increase or decrease is observed in the first-order trends of GlobColour data in more recent studies (e.g.
27 Moradi 2021). Therefore, while recognizing that some differences in regional and seasonal biases may
28 occur in unified data products and, acknowledging that discontinuities and trends of the median with time
29 should be interpreted carefully according to the sensors used (Garnesson et al., 2019), merged Chl can be
30 generally considered a good indicator of the magnitude of the overall phytoplankton trends.
31

32 *2.2 Nitrate data*

33 Since nutrient observations are still too scarce to allow obtaining time-resolved global-scale fields, we
34 used global NO₃ obtained from the biogeochemical hindcast model provided by Mercator-ocean
35 (<http://marine.copernicus.eu>, see Fig. S1). Data on climate indices were obtained from available

36 databases. Bi-monthly Multivariate El Niño Southern Oscillation Index (MEI.v2), hereafter ENSO index,
37 was obtained from the National Oceanic and Atmospheric Administration National Center for
38 Environmental Prediction website (<https://www.esrl.noaa.gov/psd/enso/mei/>). MOC data (Smeed et al.,
39 2019; Moat et al., 2022) for the period (2004-2018) was obtained from the RAPID-WATCH MOC
40 monitoring project (www.rapid.ac.uk/rapidmoc).obtained using the PISCES model (Aumont et al.,
41 2015). The model is forced by daily mean fields of ocean, sea ice, and atmospheric conditions. Ocean and
42 sea ice forcings are obtained from the numerical simulation FREEGLORYS2V4 produced at Mercator-
43 Ocean and the source of atmospheric forcings is the ERA-Interim reanalysis produced at ECMWF. Initial
44 conditions are set from the World Ocean Atlas 2013 climatology. A complete model description can be
45 found at (<http://cmems-resources.cls.fr/documents/>).

46

47 *2.3 Climatological data*

48 We compared available observational nutrient data (NO₃) from the upper 20 m of the water column,
49 obtained by merging bottle cast data from the World Ocean Database (WOD18, Boyer et al., 2018;
50 <https://www.nodc.noaa.gov/>), with model results. Generally, we found good agreement between nitrate
51 in situ data and model results ($r=0.98$). Main deviations occur in the Southern Ocean where NO₃
52 concentrations are slightly overestimated (up to 7.2 mmol m⁻³) and in some coastal areas affected by river
53 runoff.

54

55 *2.4 Identification of HNLC regions*

56 Presently, the best approximation to define the global distribution of HNLC regions in the world ocean is
57 the use of NODC maps of surface nutrients (<https://www.nodc.noaa.gov/>). However, excess nutrient
58 availability by itself does not necessarily reflect HNLC conditions. In situ experiments are capable to
59 discern Fe limitation conditions but a more manageable metric to assess the limits on the spatial extent of
60 HNLC regions is required, in particular for remote sensing applications, as well as for allowing objective
61 comparison between different environmental scenarios and studies.

62 To obtain a quantitative criterion for the definition of HNLC regions, we analyze the values of NO₃:Chl
63 ratios (mmol/mg) obtained from the SOM analysis on the time domain over the global ocean throughout
64 the 20 years of data to identify a common statistical behavior representing HNLC conditions. In
65 particular, we analyze the probability density function (*pdf*) of the extracted SOM NO₃:Chl temporal
66 patterns to identify a threshold for defining HNLC conditions (P_{HNLC}). We use the changes in the trend
67 of the standard deviation calculated for each bin of the *pdf* function set the threshold ratio. To calculate

68 the total extent of each region (km²) the spatial area of each pixel was calculated, by considering its
69 latitude.

70 *2.5 Time and space domain SOM analyses*

71 We use SOM (Kohonen, 1982) to elucidate spatial and temporal patterns in the complex relationship
72 between nutrients and phytoplankton. SOM is a subtype of artificial neural network that uses an
73 unsupervised machine learning algorithm to process and extract hidden structures in large datasets. The
74 SOM algorithm is mainly based on a training process through which an initial neural network is
75 transformed by iteratively presenting the input data. In this study, the architecture of the neural network
76 is set in a sheet hexagonal map lattice of neurons, or units, to have equidistant neurons, and to avoid
77 anisotropy artifacts. Each neuron is represented by a weight vector with a number of components equal
78 to the dimension of the input data vector, i.e. number of rows or columns in the Chl and NO₃ matrices,
79 depending on whether the analysis is performed in the temporal or in the spatial domain. We use an initial
80 network composed of units of random values (random initialization). In each successive iteration during
81 the training process, the neuron with the greatest similarity (excited neuron), called Best Matching Unit
82 (BMU), is updated by replacing their values with the Chl and NO₃ values of the input sample data. The
83 similarity is estimated by computing the Euclidean distance between the components of the input sample
84 and the components of the weight vector of the unit. The unit most similar to the input sample is the one
85 with the minimum distance. In the learning process, Chl and NO₃ values of the topological neighboring
86 neurons of the excited neuron (BMU) are also updated replacing their values with values determined by
87 a Gaussian neighborhood function. In these computations, we use the imputation batch training algorithm
88 (Vatanen et al., 2015) where the SOM assumes that a single sample of data (input vector) contributes to
89 the creation of more than one pattern, as the whole neighborhood around the best-matching pattern is also
90 updated in each step of training. This yields a more detailed assimilation of particular features appearing
91 on neighboring patterns. A final neural network with the NO₃:Chl patterns is obtained after repeating the
92 training process until a stable convergence of the map is obtained.

93 For typical satellite datasets, the SOM can be applied to both space and time domains. By applying the
94 SOM in the spatial domain, one can extract characteristic spatial patterns of the input data. If transposing
95 the input data matrix and applying the SOM in the time domain, one can extract characteristic temporal
96 patterns, i.e., the characteristic time series. Since each of these time series represents the temporal
97 variability of a particular region, this method can be used to identify regions of differentiated variability
98 on a map. The SOM, when applied to both space and time domains of the same data (called "dual SOM"
99 analysis by Liu et al. 2016), provides a powerful tool for diagnosing ocean processes from such different
00 perspectives. In this study we focus on the second type. We have addressed the analysis separately in the
01 time and space domains of the log-transformed NO₃ and Chl datasets. In the time domain, we implement

02 a [4x3] joint-SOM analysis of NO₃ and Chl using as input weight vectors concatenating the time-series
03 of NO₃ and Chl at each pixel, so each neuron corresponds to a characteristic joint NO₃ and Chl temporal
04 pattern over the total period of data. Since each pixel has an associated characteristic time series, we can
05 obtain the location of a particular temporal pattern by computing the BMU for each pixel, providing a
06 map of regions of differentiated NO₃:Chl temporal variability. For the analysis herein presented only the
07 regions with NO₃:Chl > P_{HNL}C are considered (regions R1 to R5).

08 An obstacle to the temporal domain analysis on a global scale is the opposed seasonality in both earth's
09 hemispheres. The algorithm classifies the time series at each grid point attending to the period of the
10 signal but does not consider time lags between the time series. Hence, pixels located either in the northern
11 or in the southern hemisphere displaying a similar significant period in the NO₃ and Chl temporal
12 variability are classified in the same regional pattern even if they are in antiphase when the signals are
13 seasonally lagged (6 months delayed). Regionalization is spatially coherent but the seasonal variation in
14 the characteristic pattern that represents the neuron mixes the phenological patterns of both hemispheres.
15 Therefore, to properly analyze the properties and trends of each of the classified regions, we have
16 calculated the mean features of the regions by segregating the grid points corresponding to each pattern
17 obtained from the SOM analysis into the northern, equator, and southern hemispheres (see scheme in
18 Fig.1). Linear trends of NO₃ and Chl concentrations in each region are estimated by decomposing the
19 NO₃:Chl time series in a seasonal signal plus a residual component and applying Theil-Sen slope
20 adjustment (Sen, 1968) of the residuals of the deseasonalized series. Correlation analyses were performed
21 using the Pearson Product Moment correlation computing best-fit linear trends using regression analysis.

22 The SOM analysis in the spatial domain [3x3] array, is addressed by using as input data weighted vectors
23 consisting of spatial distributions over the global ocean of NO₃:Chl ratios at a particular time. The
24 selection of the number of neurons depends on the complexity of the data, on the features to be examined
25 in the dataset, and on the minimization of the errors. In this case, the resulting neurons after the training
26 loop unveil the characteristic patterns describing the spatial variability of the HNL regions on a global
27 scale. Then, when computing the BMU for each time we designate the extracted characteristic spatial
28 pattern that better describes the spatial distribution of NO₃:Chl ratios (P1 to P9) at each time, obtaining
29 the time evolution of the characteristic spatial patterns throughout the considered period.

30 Because the SOM is based on the similarity computed from the Euclidean distance between samples, the
31 input vectors of the different variables are normalized to the same range, before initializing the SOM
32 computations. This guarantees a consistent comparison of the weights of the components when computing
33 the distance of two vectors.

34 The size of the neural network (number of neurons) depends on the number of samples and on the
35 complexity of the patterns and an optimal choice is important to maximize the quality of the SOM. In the
36 present study, the map size is set to be [4 x 3] with 12 neurons for the time domain analysis, and a [3 x 3]
37 neural network is used in the spatial domain. Using larger map sizes, the patterns are slightly more
38 detailed, and more regions of a particular variability emerge, but the occurrence of the probability of the
39 patterns decreases, without affecting the results noticeably (Basterretxea et al., 2018; Hernandez-Carrasco
40 and Orfila, 2018). If a reduced neural map, such as [2 x 2] is used, patterns are concentrated together with
41 the occurrence probability in a few rough patterns but increasing, in this case, the topological error.

42 SOM computations have been performed using the MATLAB© toolbox of SOM v.2.0 (Vensanto et al.,
43 1999) provided by the Helsinki University of Technology (<http://www.cis.hut.fi/somtoolbox/>). Further
44 information on SOM analysis is provided in the supplementary materials.

45

46 *2.6 Combined SOM - wavelet coherence analysis*

47 Joint SOM-wavelet power spectral analysis was demonstrated by Liu et al. (2016) in the study of
48 characteristic time series of sea level variations in different regions of Gulf of Mexico. Here in this study,
49 we expand it further to combined SOM-wavelet coherence analysis to assess the response of HNLC
50 regions to global forcings we use an approach based on the wavelet coherence analysis (WCA) between
51 two time-series (Grinsted et al., 2004; see Supplementary Material for further details). WCA characterizes
52 cross-correlations by identifying the main frequencies, phase differences, and time intervals over which
53 the relationship between the variability of HNLC regions and the main global forcings considered in this
54 study, ENSO and MOC indexes, is strong. To do so, we first analyze the variability in both frequency and
55 time of the characteristic time series of NO₃:Chl in the different HNLC regions extracted by the time
56 domain SOM computations and the time series of the global forcings using the continuous wavelet
57 transform (CWT).

58 Cross-wavelet transform (XWT) characterizes the association between the CWT of two signals, providing
59 information on the common power and relative phase in the frequency-time domain of two time-series.
60 By applying the XWT to the NO₃:Chl ratios and climate forcings, we determine the cyclic changes in
61 each of the HNLC regions and their relationship with the global forcings mentioned above. Finally, we
62 quantify the correlation between the continuous wavelet transform of two signals using the wavelet
63 coherence analysis (WCA), In the time-frequency space the wavelet coherence coefficient R^2 is calculated
64 as the squared absolute value of the smoothed cross-wavelet spectrum normalized by the product of the
65 smoothed wavelet individual spectra for each scale (Torrence and Compo, 1998; Torrence and Webster,
66 1999; Grinsted et al. 2004). R^2 is interpreted as a localized correlation coefficient in the frequency-time

67 domain and it takes values between 0 (no correlation) and 1 (perfect correlation). The statistical
68 significance level of the wavelet coherence is estimated using Monte Carlo methods as described in
69 Grinsted et al. (2004). We use the MATLAB software package (Grinsted et al., 2004) for wavelet
70 coherence analysis. It should be noted that cross-wavelet analysis does not establish causative
71 relationships but only allows identifying possible linkages between variables through the synchrony of
72 their time series.

73

74 **3 Results**

75

76 *3.1 Global characterization of HNLC regions*

77 The mean pattern of global ocean color data for the 20 years analyzed reveals the well-known contrast in
78 phytoplankton biomass between the highly productive areas located in high latitudes and coastal
79 upwelling regions, and the low-latitude oceanic waters where mean values are $<0.1 \text{ mg m}^{-3}$ (Fig. 2). Low
80 Chl regions generally correspond with low surface NO_3 concentrations whereas the opposite relationship
81 (high nitrate and high chlorophyll) is not more exceptional. Indeed, nutrient-rich productive waters are
82 mainly restricted to shelf regions (coastal upwelling regions and shelf seas), or to the vicinity of islands
83 (i.e. Falkland Islands) and other topographical features where multiple and overlapping sources of other
84 elements, such as trace metals, are abundant (e.g. Boyd and Ellwood, 2010). As shown in figure 2, only
85 in the North Atlantic, the Bering Sea, and the eastern region of the Antarctic Peninsula, Chl is enhanced.
86 Conversely, a large part of surface ocean waters, particularly in the Southern Ocean and in the Equatorial
87 Pacific, correspond to regions of relatively low Chl concentrations but with excess nitrate (i.e. $>4 \text{ mmol}$
88 m^{-3}).

89 The analysis of the normalized *pdf* of the NO_3 :Chl extracted from the temporal SOM analysis (shown in
90 Fig. S2) provides a good discrimination criterion to define HNLC regions. As shown in figure 2b, the
91 normalized *pdf* of the NO_3 :Chl ratio displays a marked bimodal distribution with the main mode centered
92 at low NO_3 :Chl ($\sim 5 \text{ mmol mg}^{-1}$). The second mode, which corresponds to high nutrient-low chlorophyll
93 regions, is characterized by mean and standard deviation values of $\mu=24.1$ and $\sigma=6.7 \text{ mmol mg}^{-1}$,
94 respectively. A critical NO_3 :Chl ratio bounds the lower limit of this distribution and can be estimated as
95 $\mu - \sigma=17.4 \text{ mmol mg}^{-1}$. Consistently, the *pdf* bulk analysis of its associated standard deviation (*std*)
96 function also reveals a clear critical value located where the value of the slope varies (Fig. 2c). Both
97 analyses allow establishing a solid statistical criterion to infer a minimum value of NO_3 :Chl= 17 mmol
98 mg^{-1} for delimiting HNLC regions from other ocean regions. It is worth mentioning that while the *pdf* of
99 the NO_3 :Chl values obtained from the SOM analysis shows a bimodal distribution, the bulk *pdf* of the

00 raw NO₃:Chl values (i.e. without performing a SOM analysis) is unimodal. This suggests that the SOM
01 technique is able to unravel relevant structures in the data that cannot be identified using classical
02 approaches.

03 From the 12 characteristic time patterns of NO₃:Chl variability obtained in the [4 x 3] SOM analysis,
04 five display NO₃:Chl exceeding P_{HNLC} all the times (not partially) throughout the entire study period (Fig.
05 3a). These associated subregions (R1 to R5) match with the three traditionally reported HNLC regions
06 (Fig.3b). In these regions surface chlorophyll rarely exceeds 0.8 mg m⁻³ and the mean values range
07 between 0.21 mg m⁻³ and 0.5 mg m⁻³ (Table 1). The global extent of these 5 SOM-identified HNLC
08 subregions encompasses 25% of the ocean, being the SO by far the broadest region (18% of the ocean),
09 whereas SNP and EEP respectively occupy some 4% and 3% of the ocean. Besides the obvious absence
10 of HNLC regions in the northern and central Atlantic, some latitudinal asymmetries are observed in the
11 distribution of these regions. For example, the SO region extends to lower latitudes than the SNP (i.e.
12 ~40° S), loosely coinciding with the South Antarctic Zone limit (SAZ; Orsi, et al., 1995). Likewise,
13 consistent with previous studies of this region (Radenac et al., 2012), the EEP displays a larger extent in
14 the Southern Hemisphere (Fig. 3b).

15 The global pattern obtained from the coupled SOM analysis reflects a clear latitudinal zonation which is
16 mainly due to latitudinal variations in nutrient availability since while chlorophyll concentration
17 duplicates along the latitudinal gradient (R1 to R5), NO₃ increases up to 7-fold (see Table 1). It is
18 noteworthy that nutrient concentrations are generally lower in the SNP (i.e. <17 mmol m⁻³) than in the
19 SO while biomass is comparatively higher (see Table 1). Indeed, R1 in SNP only achieves the NO₃:Chl
20 criterion for HNLC regions during some periods. This region exhibits distinctive eastern and western
21 provinces, which are consistent with previous studies describing the western region as more productive
22 and variable (Imai et al., 2002).

23 Major differences among the characteristic NO₃:Chl patterns in the defined subregions are not only
24 indebted to variations in mean values but, also, to the intensified seasonal variability in higher latitudes.
25 For example, seasonality in Chl is particularly evident in R5 and, less so, in other polar subregions (Fig.
26 3b). Conversely, the seasonal component of variability in the EEP is masked by the intense short-term
27 variability.

28 An interesting feature depicted from the temporal SOM analysis is the positive trend in Chl experienced
29 in the HNLC regions located in polar areas, suggesting an increase in their productivity. Decadal
30 tendencies are in the range of 0.04 to 0.06 mg m⁻³ decade⁻¹ in the most productive subregions (R2 to R5
31 in SO and R3 in SNP) but become negligible at the equator (Table 1). A regional average indicates a Chl

32 increase of 0.6% yr⁻¹ in the SNP and a 1.9% yr⁻¹ in the SO. In the case of the SO, positive trends are
33 highly influenced by a positive Chl shift occurring at the end of 2010 (see Fig. 3).

34

35 *3.2 Spatial variability of HNLC regions*

36 The set of 9 coherent spatial patterns resulting from the SOM analysis in the space domain and their
37 respective probabilities of occurrence are shown in figure 4. The organization of the maps in the figure
38 reveals a hierarchical classification of the maps or scenarios. Most differentiated patterns, also displaying
39 the highest probability of occurrence (the probability to find a pattern similar to the input data), are located
40 in the corners of the neural network and transitional stages connecting these scenarios fill the center. For
41 example, along the top and left side scenarios (P1, P2, P3, and P4), generally occurring during winter (see
42 Fig. 4 and 5b), the SNP extends over a larger region compared to P7, P8, and P9, which display a 3%
43 decrease from the mean extent. Conversely, Fe limitation in the SO, as inferred from high NO₃:Chl ratios,
44 is markedly enhanced towards the top and right side of the figure (P4, P5, P7, P8, and P9). The extent of
45 the EEP region displays little variation. It should be noted that HNLC spatial extent and NO₃
46 concentrations are not necessarily coupled since the boundaries also depend on Chl concentration values.
47 In addition, patterns in the proximity of the Antarctic continent are, in some cases, not well-defined during
48 winter due to ice cover in this region.

49 Figure 5 displays the time-series of the BMUs and the monthly frequency of occurrence for each pattern.
50 The main feature observed is the marked seasonality in the patterns shown in figure 4. The patterns with
51 the highest probability of occurrence, P3 and P9 (100% in April and 70% in July respectively), represent
52 winter and summer situations in the northern hemisphere. P4 and P8 characterize transitions toward these
53 patterns. Other patterns such as P6 and P2 (mostly occurring in winter and summer) are rarer but become
54 more frequent after 2010 (Fig. 5a). As discussed below, this variation in HNLC regional patterns (i.e. P3
55 substitutes P1) suggests an abrupt and major transition towards more productive HNLC regions (higher
56 Chl is observed).

57 From the nine spatial patterns shown in figure 4, we estimated the seasonal and interannual variation in
58 the extent of the HNLC regions (Fig. 6). Note that this regional partitioning is made on a global scale
59 with global criteria and therefore leads to a large-scale smoothing, which could impact the values of the
60 variation of the areas. However, as this signal smoothing is common to all the areas, this should not have
61 any effect on the regional comparison of the area variation. The magnitude of these variations remarkably
62 contrasts between the equatorial and polar regions. While the extent of the EEP varies by 8.9% seasonally,
63 changes in SNP extent can exceed 100% (Figure 6). The peak in extent for the SNP corresponds to the
64 boreal spring (63% of the mean value in March). In the case of the SO, seasonality is mainly driven by

65 changes related to the ice limit in high latitudes. Indeed, the extent of the HNLC region in the boreal
66 winter is 25% lower than the mean annual extent.

67 A remarkably good inverse correlation ($r=-0.97$, $n=20$) is observed between the interannual variations in
68 the extent of EEP and the SO, and a weaker though significant relationship exists between the SNP and
69 the EEP ($r= -0.50$, $n=20$). Therefore, as the extent of HNLC in polar regions contracts (biomass increases),
70 the equatorial region expands and vice versa. All three regions exhibit a shift in their extent after 2010
71 (Fig. 6). Both the SNP and the SO decrease after this year (5% and 2.6%) whereas the extent of the EEP
72 slightly increases (0.4%).

73

74 *3.3 Climate drivers of HNLC region temporal variations*

75 The WCA between NO₃:Chl ratio in each HNLC region and ENSO are shown in figures 7a1 to a3.
76 Generally, small coherence structures are observed at semiannual periods; however, the main coherence
77 pattern corresponds to a band extending in the 2 to 4 years in the SNP and > 2yr in the EEP. This coherence
78 between NO₃:Chl and ENSO in the 2-4 year period is particularly clear after the year 2005 when ENSO
79 variability intensified. In the EEP, the coherence between both series expands to periods >4 years but,
80 unlike in the SNP region where the NO₃:Chl ratio is in-phase with ENSO signal, the signals are strongly
81 anticorrelated in this case (anti-phase: relative phase of 180° between both signals).

82 As in the case of ENSO, the MOC presents strong seasonal and interannual variations but it is also
83 expected to play a more active role at longer timescales (i.e. decadal and multidecadal; Buckley and
84 Marshall, 2016). Figure 7b shows the MOC transport index (hereafter MOI) measured at 26.5°N (Smeed
85 et al., 2019). Transport exceeds 17 Sv until 2009, but it weakens during 2010, stabilizing thereafter.
86 Generally, the MOI displays intense interannual variability, and coherence with NO₃:Chl ratios is
87 strongest at interannual time scales (1-1.5 yr; Fig. 7b1 to b3). At this timescale, it influences NO₃:Chl
88 ratios in the three HNLC regions yet it is more intense in the SO.

89

90 **4 Discussion**

91 *4.1 Global characterization of HNLC regions*

92 In the present study, we have addressed the analysis of the extent of the HNLC regions, their long-term
93 variability, and the potential drivers of these variations. Despite the relevance of precise characterization
94 of the extent of this biome for the estimation of the amount of carbon drawn into the ocean by
95 phytoplankton, objectively determining the boundaries of HNLC regions has remained elusive as it

96 requires coherent information from both nutrient and Chl fields. We demonstrate that a statistical
97 approach, based on a threshold in the distribution of the global NO₃:Chl ratios (P_{HNLC}), can robustly
98 discriminate these regions. As in precedent studies (e.g. Moore et al. 2013), we assume that excess NO₃
99 in surface oceanic areas is indicative of Fe limitation. This avoids relying on the scarce information
00 available on Fe-stress or in more complex ecosystem modeling approaches. Inference of phytoplankton
01 Fe-stress from satellite ocean color data has been attempted but it is a methodology that still presents large
02 uncertainties (Browning et al., 2014). Furthermore, while bioavailable Fe is known to be the primary
03 limiting factor in this relatively unproductive biome, the establishment of HNLC conditions is influenced
04 by various other factors such as light availability, grazing pressure, rate of Fe-remineralization, and
05 community structure, highlighting the complex interrelations among these factors. Despite these
06 drawbacks, the herein-developed method provides results consistent with previous descriptions of the
07 large-scale spatial patterns of HNLC regions, mostly based on NO₃ fields (i.e. Archer and Johnson, 2000;
08 Ono et al., 2008; Fu and Wang, 2022). Also, the proposed method for biome definition may introduce a
09 bias in that the resulting spatial fields are smoother compared to those based on Fe-limitation, which is
10 due to the greater variability of Fe concentrations compared to NO₃ fields.

11 The P_{HNLC} obtained from the *pdf* distribution of the NO₃:Chl ratios represents a statistical threshold that
12 integrates complex biological processes, including competition for resources, grazing, changes in species
13 composition, nutrient uptake rates, Fe-regulated algal photochemistry, etc. Unlike Redfield or C:Chl
14 ratios which respond to physiological factors within phytoplankton cells, P_{HNLC} can be considered an
15 environmental indicator of changes in the structure and functioning of marine phytoplankton.

16 According to our analysis, some 25% of the ocean (18% of the Earth's surface) corresponds to
17 unproductive HNLC waters. With 83% of the global HNLC biome extent (Table 2), the SO is the largest
18 region presenting clear latitudinal variation in the characteristic Chl patterns, as obtained from SOM
19 analysis (Fig. 3). This is consistent with available descriptions of the physical and chemical properties of
20 the SO which tend to be across latitude due to the meridional structure of the MOC and because of the
21 rapid zonal redistribution imposed by circumpolar currents (Orsi et al., 1995). Both the SNP and the EEP
22 respectively constitute 8% of the total HNLC extent. However, while the EEP remains relatively stable
23 ($cv=5$; Table 2) the SNP can change up to 2-fold (Fig, 4 and Table 2).

24 Our analysis reveals marked decadal tendencies in Chl in the most productive subregions, ranging
25 between 0.04 to 0.06 mgChl m⁻³ decade⁻¹, and negligible trends in the EEP (Table 1). Positive
26 phytoplankton trends in high latitudes and no significant tendencies in the equator at the 95% interval
27 have been previously reported by Hammond et al. (2017). Indeed, climate change projections for the 21st
28 century predict declines in global marine net primary production but increasing Southern Ocean
29 productivity (Hauck et al. 2015; Moore et al., 2018). Nevertheless, it is noteworthy that our analysis shows

30 that trends in some regions of the southern hemisphere are influenced by a Chl shift occurring in 2019-
31 2010 (particularly R4 and R5). This non-linear enhancement in phytoplankton, which is not exclusive to
32 oceanic Fe-limited waters (see for example Marrari et al., 2017), positively biases the Chl increase rate
33 in these subregions. It is unlikely that this change in overall phytoplankton biomass is related to satellite
34 data merging. SeaWiFS ended operations in 2010 and MERIS sensor ceased in April 2012; however, a
35 decrease in biomass would be expected from these changes (Garnesson et al., 2019). The possible source
36 of this shift in phytoplankton biomass is more extensively discussed below.

37

38 *4.2 Spatial variability of HNLC regions*

39 SOM analysis allowed the characterization of the seasonal and interannual variability of HNLC regions
40 (Fig 5 and 6). The SO and the SNP are regions of seasonal extremes in productivity as a consequence of
41 the large fluctuations in the environment that they experience. Important seasonal variability is observed
42 in the SO, which is attributed to light limitation during winter and to variations in iron stocks occurring
43 in surface waters (Tagliabue et al., 2014). Therefore, while presenting HNLC characteristics for most of
44 the year, the SO exhibits distinct Chl variability patterns that are well captured in the SOM regionalization
45 and the characteristic patterns of each subregion. In the case of the SO, the changes in the extent are
46 reduced (20% from mean values) which is attributed to the large-scale nature of the physical processes
47 regulating the productivity of this region (Cullen, 1991). Mid-depth and deep ocean waters communicate
48 with the ocean surface after following long a circuit route driven by ocean overturning circulation
49 (Lumpkin and Speer, 2007). As reported by Smeed et al. (2018), the variability of the MOC flow system
50 has an important decadal component associated with thermohaline forcing. This long-term component of
51 variability could dominate over higher frequency variability but the length of the observational record of
52 the AMOC is still insufficient to resolve variations at this scale.

53 Variability patterns in the SNP, are attributed both to marked seasonality in the local forcings and to
54 fluctuations in the regional circulation patterns and the consequent advective Fe enrichment processes
55 from river discharges of the surrounding marginal regions in the North Pacific (Cummins and Freeland
56 2007; Takeda, 2011; Lauderdale et al., 2020; Nishioka et al., 2020). In the Northern Pacific, surface Fe
57 availability is driven by vertical mixing processes which closely relate to seasonal variations in weather
58 conditions (Nishioka et al., 2007; 2020). Upwelling is triggered by severe winter cyclones that generate
59 enough Ekman pumping to maintain high nutrient concentrations in the near-surface waters (Gargett,
60 1991; Harrison et al., 2004).

61 Marked differences in variability are observed between the subpolar regions and the EEP, where
62 seasonality is marginal. Nevertheless, it should be noted that the EEP is a peculiar region that integrates

63 subregions with 6-month out-phased seasonal variations (north and south of the equator). On average, the
64 south-equatorial region contributes more (62% of the total extent) to the mean extent of the EEP whereas
65 the Northern subregion determines most of the observed variability (Fig. S3).

66 At interannual scales, the extent of HNLC regions is more modest (up to 5%; Figure 6) but all three
67 regions are notably correlated, suggesting that their interannual variations are driven by global-scale
68 processes. In particular, the SO and the EEP are highly correlated ($r=0.97$). This coupling between
69 Southern Ocean productivity, and equatorial productivity, was suggested by Dugdale et al. (2002) based
70 on the observed nutrient ratios. They proposed that both regions were connected, out of phase, by the
71 meridian SubArctic Mode Water. Nevertheless, the seaways in the Pacific are complex, and determining
72 the overturning signature is challenging. Some studies have suggested that temperature anomalies
73 subducted into the pycnocline at subtropical latitudes may not reach the Equator with any appreciable
74 amplitude (Schneider et al., 1999a). However, mass water balances in the equatorial Pacific reveal that
75 the strength of the equatorial upwelling is related to variations in the Pacific overturning (PMOC)
76 (McPhaden and Zhang, 2002), and therefore, an influence on EEP extent is expected. Likewise,
77 meridional circulation extends to the North Pacific; however, the SNP does not ventilate the deep ocean
78 at significant rates and the PMOC cell at this latitude corresponds to a rather independently functioning
79 intermediate water cell (Warren et al., 1983). MOC in this region is reportedly weak (1-4 Sv) and extends
80 no further than 50°N (Ishizaki, 1994; Yaremchuk, 2001). However, there is evidence showing the
81 response of this region to changes in PMOC (Burls et al, 2017, Holzer et al, 2021). For example, it has
82 been observed in TOPEX altimeter data that MOC influences the basin-scale baroclinic circulation in the
83 SNP (Kuragano and Kamachi, 2004). This would explain the lower, yet significant, correlation with the
84 variations at the SO and EEP. Indeed, the shift observed in 2009-2010 is common to all three regions
85 (albeit with a different sign).

86 The causes of the drastic 2009-2010 variation in the extent of HNLC regions are uncertain but they can
87 plausibly be related to changes in the strength of meridional circulation and the consequent atmospheric
88 and oceanic variations. For example, Moat et al. (2020) suggest a previously unsuspected role for the
89 AMOC in climate variability during the 2010 event which coincided with a cold winter in Europe. Several
90 ocean scale changes that may be related to the observed changes in the HNLC region extent have been
91 reported in the period 2009-2011. For example, rapid warming, salinification, and a concurrent dissolved
92 oxygen decline have been observed at BATS during the 2010s (Bates and Johnson, 2020). There is also
93 evidence indicating that a decadal intensification of Pacific trade winds weakened in 2011 (Bordbar et
94 al., 2019). Trade wind intensity variations in the equatorial Pacific region are associated with SST
95 anomalies, weakening of the equatorial divergence, and changes in upper-ocean thermal structure
96 (England et al., 2014; Bordbar, et al., 2017). The relationship between the equatorial wind intensity and

97 the equatorial undercurrent strength is also well established (McPhaden, 1993). These atmospheric
98 changes, affecting the upwelling of Fe in the EEP (and indirectly to other oceanic regions), agree with the
99 hypothesis of Winckler et al. (2016) suggesting that ocean dynamics, not dust deposition, control the
00 equatorial Pacific productivity. In our case, we observe a reduction of the extent of the HNLC region in
01 the EEP during an enhanced wind intensity period (before 2011) and an expansion thereafter (Fig. 6).
02 Connections of this mechanism to high latitude HNLC regions reveal large-scale adjustments with
03 consequences in global ocean productivity.

04

05 *4.3 Drivers of HNLC region variability*

06 ENSO is the primary source of the interannual variability in this region and its occurrence is related to
07 the decline in NO₃ supply. Sub-decadal fluctuations in Chl in the EEP region displaying a good
08 correlation with the ENSO index have been reported before (Oliver and Irwin, 2008; Boyce et al., 2010).
09 By contrast, the SO only shows weak evidence of this relationship which suggests that ENSO is not a
10 major forcing driving the variability of NO₃:Chl in this region. This is consistent with reports from Ayers
11 and Strutton (2013) who did not find a significant relationship between nutrients in this region and ENSO
12 events. Similarly, Racault et al. (2017) reported evidence indicating that during Eastern Pacific and
13 Central Pacific types of El Niño events, impacts on phytoplankton were widespread, but tended to be
14 greatest in the tropics and subtropics, encompassing up to 67% of the total ocean affected areas.

15 It can be argued that differences in the response to ENSO are due to the different nature of the forcings
16 driving nutrient supply in each region. While the EEP and the SNP seem to respond to ENSO-related
17 changes in wind forcing, NO₃:Chl ratios in the SO are more stable and respond to annual and semi-annual
18 variations. The coupling between the EEP and the SNP dynamics has been reported before. Qiu (2002)
19 observed progressive shoaling of the Alaska gyre caused by a strengthening of the cyclonic circulation.
20 The interannual variability of this gyre was connected to ENSO-related equator-originated sea surface
21 height anomalies. Several large-scale climate pattern indexes are invoked to explain physical and
22 biological fluctuations in the SNP. For example, Di Lorenzo et al., (2008) defined the North Pacific Gyre
23 Oscillation (NPGO), which nicely explains the fluctuations of salinity, nutrients, and chlorophyll related
24 to the circulation in the North Pacific gyre. It is beyond the scope of the present work to assess the
25 relationships of all these indexes with the variability in the extent of HNLC regions. Nevertheless, the
26 proposed climate indexes for the Pacific present a high relationship among them, which highlights the
27 strong dynamical linkages between tropical and extratropical modes of climate variability in the Pacific
28 basin, and the important role played by ENSO (Di Lorenzo et al., 2013).

29 A stronger MOC should result in the upwelling of macronutrients and Fe at faster rates as well as in
30 increased Ekman transport of nutrients equatorward and subsequent subduction (Ayers and Strutton,
31 2013). This is observed in the high positive cross-wavelet correlation at 1-1.5 yr in the EEP region. In
32 addition, a clear variation in the coherence phase is observed, being 90° (3-4 months) in the SNP, in phase
33 for the EEP, and 270° (9-11 months) out of phase in the SO, suggesting a meridional propagation of the
34 MOC effect. Figure 8b also reveals a decline of the MOC until 2010 that has remained $\sim 15\%$ below its
35 pre-2010 level since then (~ 17 Sv; Ayala-Solares et al., 2018; Caesar et al., 2018). This trend has been
36 attributed to climate warming and the consequent changes in the hydrological cycle, including sea-ice
37 loss and accelerated melting of the Greenland Ice Sheet, causing further freshening of the northern
38 Atlantic (Bakker et al., 2016; Böning et al., 2016). It has been proposed that AMOC weakening will affect
39 large regions of the world's upper oceans that are currently supplied with nutrients by the South Antarctic
40 Mode Water (Schmittner, 2005).

41 Weakened MOC after 2010 and, the particularly low value during that year (Fig. 7b), is coincident with
42 the shift in the extent of the HNLC regions shown in Figure 5, suggesting that weaker MOC is related to
43 increases in the extent of the EEP and contraction of the SNP and the SO HNLC regions. In the case of
44 the EEP, it could be proposed that a larger equatorial area with Fe deficiency would be associated with a
45 decline in upwelling intensity. It is estimated that the slowing down of the overturning circulation in the
46 Pacific Ocean since the 1970s has generated a decrease in upwelling of about 25% in an equatorial strip
47 between 9° N and 9° S (McPhaden and Zhang, 2002). Nevertheless, the larger HNLC region in the EEP
48 could also be explained by the depletion of Fe in the source waters feeding the EUC, as reported by Kaupp
49 et al. (2011).

50 At high latitudes, the weakening of the AMOC, is coherent with a decrease in the extent of the SNP and
51 the SO (Fig. 5). This anomaly, starting in 2009-2010, is a global feature also reflected in the intertropical
52 convergence zone (ITCZ) time series, an atmosphere's energy balance indicator (see Green et al., 2017;
53 Ibanhez et al., 2017), suggesting a strong atmosphere-ocean coupling with impact on ocean productivity.
54 It is not clear how a reduced flow would favor the increase in biomass in high latitudes. While it is
55 plausible that in the case of abrupt and/or permanent variations of AMOC primary production, and hence
56 phytoplankton biomass, will be reduced, it is less clear how present-day variations influence
57 phytoplankton biomass. It has been proposed that a reduced AMOC from increased precipitation and
58 melting sea ice, could contribute to reduce vertical mixing which may increase productivity in polar
59 regions (Riebesell et al., 2009). Other studies (e.g., Martinez-García et al., 2009), showed a relationship
60 between AMOC and Chl variations, mainly due to the interaction of the main pycnocline and the upper
61 ocean seasonal mixed layer. In addition, some paleoclimatic studies have demonstrated that AMOC
62 weakening can increase the productivity north from the Polar Front, but only if an increase in the

63 atmospheric soluble Fe flux is considered (Muglia et al., 2018). Paleoceanographical records reveal a
64 strong correlation between proxies of aeolian Fe flux and productivity has been reported in this region
65 (Kumar et al., 1995; Martínez-García et al., 2009) but, in present times, dust deposition in this area has
66 notably varied and this effect is unlikely to be important at the time scales considered here. Complex
67 ecosystem processes including competition for Fe with bacteria, Fe remineralization rates, and organic
68 complexation processes could determine the phytoplankton response under future scenarios. Further,
69 biomass building up is not only driven by nutrient availability. Changes in biomass can be produced by
70 variations in the thermocline depth affecting the vertical distribution of phytoplankton. Nevertheless,
71 variations in phytoplankton composition, physiological adjustments in cellular pigmentation, and grazing
72 could also modulate Chl variability. Indeed, the prevailing foodweb structure may play an important role
73 in Fe fertilization (Schmidt et al., 2016). At larger scales, there are still unresolved questions about the
74 couplings occurring at different temporal scales. For example, MOC variations are known to interact with
75 ENSO variability (Dong et al., 2006; Dong and Sutton, 2007; Timmermann et al., 2007). These
76 connections provide further evidence of the global scale coupling and feedback between the atmosphere,
77 the ocean, and global productivity variations.

78

79 **5. Conclusions**

80 Variations in the boundaries of the HNLC regions can provide an integrative view of how climate scale
81 ocean variations influence ocean productivity. We established a statistical criterion to identify HNLC
82 regions from global Chl and NO₃ data that sets the basis for systematic analyses of HNLC regions and
83 their response to climate variations.

84 Our results suggest that while local-scale processes can determine certain aspects of the productivity of
85 HNLC regions, their long-term patterns are strongly influenced by variations in global atmospheric and
86 oceanic circulation. We observed significant interannual variations in the extent of HNLC (up to 5% in
87 Fig. 6), which are associated with anomalies in global forcing intensity. Accordingly, our findings suggest
88 a scenario in which HNLC regions are vulnerable to interbasin teleconnections rather than local forcings.
89 These general patterns may be modulated by feedback between different forcing mechanisms. For
90 instance, there is a positive correlation between PMOC variability and El Niño-Southern Oscillation
91 (Tandon et al. 2020). Furthermore, our analysis reveals a shift in phytoplankton biomass and HNLC
92 variation patterns occurring at the end of 2010, which evidences the occurrence of fast transitions in ocean
93 biogeochemistry. The underlying drivers of these regime shifts and the resulting biological responses to
94 these ocean-scale changes require further investigation since they are a fundamental aspect of long-term
95 variations in marine ecosystem functioning.

96 Finally, the present study highlights the importance of maintaining long and coherent datasets beyond
97 satellite-borne information to be able to disentangle the different components of variability, particularly
98 at long timescales, and to evaluate the impact of climate change on marine ecosystems. Most of the
99 geochemical information at this scale (i.e. nutrient and Fe fields) will probably require further global
00 sampling programs and refined modeling.

01 **Author contributions**

02 Data were processed and analyzed mainly by G.B., J.S.F, and I.H-C. Writing by G. B., J.S.F, and I. H-C.
03 and S.A.S. The authors declare no competing financial interests.

04 **Funding sources and data references**

05 This work was partially supported by SIFOMED grant (CTM2017-83774-P) from Ministerio de Ciencia,
06 Innovación y Universidades, the Agencia Estatal de Investigación (AEI), and the Fondo Europeo de
07 Desarrollo Regional (FEDER, UE). G. Basterretxea was supported by Salvador de Madariaga
08 PRX18/00056 scholarship. J.S Font-Muñoz acknowledges funding by an individual postdoctoral
09 fellowship “Margalida Comas” (PD/018/2020) from Govern de les Illes Balears and Fondo Social
10 Europeo. I. Hernandez-Carrasco acknowledges financial support from the project TRITOP (grant
11 UIB2021-PD06) funded by Universitat de les Illes Balears and FEDER (EU).

12

13 All data included in the present study is accessible from the following publicly available repositories:
14 CARINA (<https://www.nodc.noaa.gov/ocads/oceans/CARINA/>), COPERNICUS
15 (<https://marine.copernicus.eu/>), ECMWF (<https://www.ecmwf.int/>), GEOTRACES
16 (<https://www.geotraces.org/>), GlobColour (www.globcolour.info), MERCATOR ([https://cmems-
17 resources.cls.fr/](https://cmems-resources.cls.fr/)), NERC (<https://nerc.ukri.org>) and NOAA (<https://www.nodc.noaa.gov/>).

18 **References**

19 Archer, D., Johnson, K.S.: A model of the iron cycle in the ocean. *Global Biogeochemical Cycles*, 14, 269-279. doi:
20 10.1029/1999GB900053, 2000.

21 Aumont, O., Éthé, C., Tagliabue, A., Bopp, L., & Gehlen, M.: PISCES-v2: an ocean biogeochemical model for carbon and
22 ecosystem studies. *Geoscientific Model Development Discussions*, 8(2), 1375-1509, 2015

23 Ayers, J.M., Strutton, P.G.: Nutrient variability in Subantarctic Mode Waters forced by the Southern Annular Mode and ENSO.
24 *Geophysical Research Letters*, 40, 3419–3423. doi: 10.1002/grl.50638, 2013

25 Ayala-Solares, J.R., Wei, H.L., Digg, G.R.: The variability of the Atlantic meridional circulation since 1980, as hindcast by a
26 data-driven nonlinear systems model. *Acta Geophysica*, 66, 1-13. doi: 10.1007/s11600-018-0165-7, 2018.

27 Bakker, P., Schmittner, A., Lenaerts, J.T.M., Abe-Ouchi, A.: Fate of the Atlantic Meridional Overturning Circulation: strong
28 decline under continued warming and Greenland melting. *Geophysical Research Letters*, 43, 12252–12260. doi:
29 10.1002/2016GL070457, 2016.

30 Basterretxea, G., Font-Muñoz, J. S., Salgado-Hernanz, P. M., Arrieta, J., & Hernández-Carrasco, I.: Patterns of chlorophyll
31 interannual variability in Mediterranean biogeographical regions. *Remote sensing of environment*, 215, 7-17, 2018

32 Bates N.R., Johnson, R.J.: Acceleration of ocean warming, salinification, deoxygenation and acidification in the surface
33 subtropical North Atlantic Ocean. *Communications Earth & Environment*, 1, 33, doi:10.1038/s43247-020-00030-5, 2020.

34 Bertrand E.M., Saito M.A., Lee P.A., Dunbar R.B., et al.: Iron limitation of a springtime bacterial and phytoplankton
35 community in the Ross Sea: implications for vitamin b12 nutrition. *Frontiers in Microbiology*, 2, 160.
36 doi:10.3389/fmicb.2011.00160, 2011.

37 Bertrand, E.M., Allen, A.E., Dupont, C.L., Norden-Krichmar, T.M., et al.: Influence of cobalamin scarcity on diatom molecular
38 physiology and identification of a cobalamin acquisition protein. *Proceedings of the National Academy of Sciences*, 109 (26),
39 E1762-71. doi: 10.1073/pnas.1201731109, 2012.

40 Böning, C.W., Behrens, E., Biastoch, A., Getzlaff, K. Bamber, J. L.: Emerging impact of Greenland meltwater on deepwater
41 formation in the North Atlantic Ocean. *Nature Geoscience*, 9, 523–527. doi: 10.1038/ngeo2740, 2016.

42 Bordbar, M.H., Martin, T., Latif, M., Park W.: Role of internal variability in recent decadal to multidecadal tropical Pacific
43 climate changes. *Geophysical Research Letters*, 44, 4246–4255. doi: 10.1002/2016GL072355, 2017.

44 Bordbar, M.H., England, M.H., Gupta, A., Santoso, A., et al.: Uncertainty in near-term global surface warming linked to
45 tropical Pacific climate variability. *Nature communications*, 10, 1990 doi: 10.1038/s41467-019-09761-2, 2019.

46 Boyce, D.G., Lewis, M.R., Worm, B.: Global phytoplankton decline over the past century. *Nature*. 466(7306), 591–596. doi:
47 10.1038/nature09268, 2010.

48 Boyd, P., Watson, A., Law, C., Abraham, E.R., et al.: A mesoscale phytoplankton bloom in the polar Southern Ocean
49 stimulated by iron fertilization. *Nature*, 407, 695–702. doi:10.1038/35037500, 2000.

50 Boyd P., Law C., Wong C, Nohiri Y. et al.: The decline and fate of an iron-induced subarctic phytoplankton bloom. *Nature*.
51 428, 549–553. doi:10.1038/nature02437, 2004.

52 Boyd, P.W., Strzpek, R., Takeda, S., Jackson, G. et al.: Mesoscale iron enrichment experiments 1993-2005: Synthesis and
53 future directions. *Science*. 315, 612–617. doi: 10.4319/lo.2005.50.6.1872, 2005.

54 Boyd, P.W., Jickells T., Law C.S., Blain S. et al.: The evolution and termination of an iron-induced mesoscale bloom in the
55 northeast subarctic Pacific. *Limnology and Oceanography*, 50, 1872-1886, 2007.

56 Boyd, P.W., Ellwood, M.J.: The biogeochemical cycle of iron in the ocean. *Nature Geoscience*, 3, 675-682. doi:
57 10.1038/ngeo964, 2010.

58 Boyer, Tim P.; García, Hernán E.; Locarnini, Ricardo A.; Zweng, Melissa M.; Mishonov, Alexey V.; Reagan, James R.;
59 Weathers, Katharine A.; Baranova, Olga K.; Paver, Christopher R.; Seidov, Dan; Smolyar, Igor V. (2018). *World Ocean Atlas*

60 2018. [Nitrate,WOD]. NOAA National Centers for Environmental Information. Dataset.
61 <https://www.ncei.noaa.gov/archive/accession/NCEI-WOA18>. Accessed [15/02/2022].

62 Browning, T.J., Bouman, H.A., Moore C.M.: Satellite-detected fluorescence: Decoupling nonphotochemical quenching from
63 iron stress signals in the South Atlantic and Southern Ocean. *Global biogeochemical cycles*. 28, 510–524. doi:10.1002/
64 2013GB00477, 2014.

65 Browning, T. J., Achterberg, E.P., Rapp I., Engel A., et al.: Nutrient co-limitation at the boundary of an oceanic gyre. *Nature*.
66 551, 242-246. doi:10.1038/nature24063, 2017.

67 Bryant, D. A.: The beauty in small things revealed. *Proceedings of the National Academy of Sciences*,100, 9647–9649. doi:
68 /10.1073/pnas.1834558100, 2003.

69 Buckley, M.W., Marshall, J.: Observations, inferences, and mechanisms of Atlantic Meridional Overturning Circulation
70 variability: A review. *Reviews of Geophysics*, 54, 54-63. doi: 10.1002/2015RG000493, 2016

71 Burls, N. J., Fedorov, A. V., Sigman, D. M., Jaccard, S. L., Tiedemann, R., & Haug, G. H.: Active Pacific meridional
72 overturning circulation (PMOC) during the warm Pliocene. *Science Advances*, 3(9), e1700156, 2017

73 Caesar, L., Rahmstorf, S., Robinson, A., Feulner G., Saba, V.: Observed fingerprint of a weakening Atlantic Ocean overturning
74 circulation. *Nature* 556, 191–196. doi: 10.1038/s41586-018-0006-5, 2018.

75 Chavez, F.P., Buck, K.R., Coale, K.H., Martin, J.H., et al.: Growth rate, grazing, sinking, and iron limitation of equatorial
76 Pacific phytoplankton. *Limnology and Oceanography*, 36, 1816–1833. doi: 10.4319/lo.1991.36.8.1816, 1991.

77 Chisholm S.W., Morel F.M.M.: What controls phytoplankton production in nutrient-rich areas of the open sea? *American-*
78 *Society-of-Limnology-and-Oceanography Symposium - 22-24 February 1991 San-Marcos, California – Preface*. *Limnology*
79 *and Oceanography*, 36, 1507-1965, 1991.

80 Coale, K.H., Johnson K.S., Fitzwater S.E., Gordon R.M., et al.: A massive phytoplankton bloom induced by an ecosystem-
81 scale iron fertilization experiment in the equatorial Pacific Ocean. *Nature*. 383, 495-501. doi: 10.1038/383495a0, 1996.

82 Coale, K.H., Johnson K.S., Chavez F.P., Buesseler K., et al.: Southern Ocean iron enrichment experiment: Carbon cycling in
83 high- and low-Si waters. *Science*. 304, 408– 414. doi: 10.1126/science.1089778, 2004.

84 Cohen, N.R., Ellis, K.A. Burns, W.G., Lampe, R.H., et al.: Iron and vitamin interactions in marine diatom isolates and natural
85 assemblages of the Northeast Pacific Ocean. *Limnology and Oceanography*, 62, 2076-2096. doi: 10.1002/lno.10552, 2017.

86 Cullen, J.J.: Status of the iron hypothesis after the open-ocean enrichment experiment. *Limnology and Oceanography*, 40,
87 1336-1343. doi: 10.4319/lo.1995.40.7.1336, 1995.

88 Cullen, J. J.: Hypotheses to explain high-nutrient conditions in the open sea. *Limnology and Oceanography*, 36(8), 1578-1599,
89 1991

90 Cummins P.F, Freeland H.J.: Variability of the North Pacific Current and its bifurcation, *Progress in Oceanography*, 75, 253-
91 265, doi: 10.1016/j.pocean.2007.08.006, 2007

92 de Baar, H.J.W., de Jong, J.T.M., Bakker, D.C.E., Löscher, B.M., et al.: Importance of iron for plankton blooms and carbon
93 dioxide drawdown in the Southern Ocean. *Nature*. 373, 412-415. doi: 10.1038/373412a0, 1995.

94 Di Lorenzo E., Schneider N., Cobb K.M., Chhak K, et al.: North Pacific Gyre Oscillation links ocean climate and ecosystem
95 change. *Geophysical Research Letters*, 35, L08607. doi:10.1029/2007GL032838, 2008.

96 Di Lorenzo, E., Combes, V. Keister, J.E., Strub, P.T., et al.: Synthesis of Pacific Ocean climate and ecosystem dynamics.
97 *Oceanography*. 26, 68–81, doi: 10.5670/oceanog.2013.76, 2013.

98 Dong, B., Sutton, R. T., & Scaife, A. A.: Multidecadal modulation of El Niño–Southern Oscillation (ENSO) variance by
99 Atlantic Ocean sea surface temperatures. *Geophysical Research Letters*, 33(8), 2006

00 Dong, B., & Sutton, R. T.: Enhancement of ENSO variability by a weakened Atlantic thermohaline circulation in a coupled
01 GCM. *Journal of Climate*, 20(19), 4920-4939, 2007

02 Dugdale R.C., Wischmeyer A.G., Wilkerson F.P., Barber R.T., et al.: Meridional asymmetry of source nutrients to the
03 equatorial Pacific upwelling ecosystem and its potential impact on ocean–atmosphere CO₂ flux; a data and modeling approach,
04 *Deep Sea Research Part II: Topical Studies in Oceanography*, 49, 2513-253, 2002

05 Dugdale, R.C., Wilkerson F.P.: Silicate regulation of new production in the equatorial Pacific upwelling. *Nature*. 391, 270-
06 273. doi: 10.1038/34630, 1998.

07 Eldridge, M.L., Trick, C., Alm, MB, DiTullio, et al.: Phytoplankton community response to a manipulation of bioavailable
08 iron in HNLC waters of the subtropical Pacific Ocean. *Aquatic Microbial Ecology*, 35, 79-91. doi: 10.3354/ame035079, 2004.

09 England, M.H., McGregor, S., Spence, P., Meehl, G. A., et al.: Recent intensification of wind-driven circulation in the Pacific
10 and the ongoing warming hiatus. *Nature Climate Change*, 4, 222–227. doi: 10.1038/nclimate2106, 2014.

11 Falkowski, P.G., Barber, R.T., Smetacek, V.: Biogeochemical controls and feedbacks on ocean primary production. *Science*.
12 281, 200-206. doi: 10.1126/science.281.5374.200, 1998.

13 Firme, G.F., Rue, E.L., Weeks, D.A., Bruland, K.W., Hutchins, D. A.: Spatial and temporal variability in phytoplankton iron
14 limitation along the California coast and consequences for Si, N, and C biogeochemistry. *Global Biogeochemical Cycles*, 17,
15 1016. doi: 10.1029/2001GB001824, 2003.

16 Fu, W., Randerson, J.T., Moore, J.K.: Climate change impacts on net primary production (NPP) and export production (EP)
17 regulated by increasing stratification and phytoplankton community structure in the CMIP5 models. *Biogeosciences*, 13, 5151-
18 5170. doi: 10.5194/bg-13-5151-2016, 2016, 2016.

19 Fu, W., Wang, W.-L.: Biogeochemical equilibrium responses to maximal productivity in high nutrient low chlorophyll regions.
20 *Journal of Geophysical Research: Biogeosciences*, 127, e2021JG006636. <https://doi.org/10.1029/2021JG006636>, 2022

21 Gargett, A. E.: Physical processes and the maintenance of nutrient-rich euphotic zones. *Limnology and Oceanography*, 36(8),
22 1527-1545, 1991

23 Garnesson P., Mangin A., Fanton d’Andon O., Demaria J., Bretagnon M.: The CMEMS GlobColour chlorophyll a product
24 based on satellite observation: multi-sensor merging and flagging strategies. *Ocean Sci.*, 15 (3), pp. 819-830 ,2019

25 Green, B., Marshall, J., & Donohoe, A.: Twentieth century correlations between extratropical SST variability and ITCZ shifts.
26 *Geophysical Research Letters*, 44, 9039–9047, doi: 10.1002/2017GL075044, 2017

27 Grinsted, A., Moore, J.C., Jevrejeva, S.: Application of the cross wavelet transform and wavelet coherence to geophysical time
28 series. *Nonlinear Processes in Geophysics*, 11, 561-566. doi:10.5194/npg-11-561-2004, 2004.

29 Hammond, M.L., Beaulieu, C., Sahu, S.K., Henson, S.A.: Assessing trends and uncertainties in satellite-era ocean chlorophyll
30 using space-time modeling. *Global Biogeochemical Cycles*, 31, 1103–1117. doi: 10.1002/2016GB005600, 2017.

31 Harrison, P. J., Whitney, F. A., Tsuda, A., Saito, H., & Tadokoro, K.: Nutrient and plankton dynamics in the NE and NW gyres
32 of the subarctic Pacific Ocean. *Journal of Oceanography*, 60, 93-117, 2004

33 Hauck, J., Völker, C., Wolf-Gladrow, D. A., Laufkötter, C., Vogt, M., Aumont, O.: On the Southern Ocean CO₂ uptake and
34 the role of the biological carbon pump in the 21st century. *Global Biogeochemical Cycles*, 29(9), 1451-1470, 2015

35 Hernández-Carrasco, I., & Orfila, A.: The Role of an Intense Front on the Connectivity of the Western Mediterranean Sea:
36 The Cartagena-Tenes Front. *Journal of Geophysical Research: Oceans*, 123(6), 4398-4422, 2018

37 Holzer, M., DeVries, T. & de Lavergne, C.: Diffusion controls the ventilation of a Pacific Shadow Zone above abyssal
38 overturning. *Nat Commun* 12, 4348, 2021

39 Howarth D.A.: An analysis of the variability of cyclones around Antarctica and their relationship to sea-ice extent. *Annals of*
40 *the Association of American Geographers*. 73, 519-537. doi:10.1111/j.1467-8306.1983.tb01856.x, 1983

41 Hutchins, D.A., DiTullio, G.R., Zhang, Y., Bruland, K.W.: An iron limitation mosaic in the California upwelling regime.
42 *Limnology and Oceanography*, 43, 1037-1054. doi: 10.4319/lo.1998.43.6.1037, 1998.

43 Hutchins D.A., Hare C.E., Weaver R.S., Zhang Y., et al.: Phytoplankton iron limitation in the Humboldt Current and Peru
44 Upwelling. *Limnology and Oceanography*, 47, 997- 1011. doi: 10.4319/lo.2002.47.4.0997, 2002.

45 Ibanez, J.S.P., Flores M., Lefèvre, N.: Collapse of the tropical and subtropical North Atlantic CO₂ sink in boreal spring of
46 2010. *Sci. Rep.* 7, 41694. doi: 10.1038/srep41694, 2017

47 Imai, K., Nojiri, Y., Tsurushima, N., Saino, T.: Time series of seasonal variation of primary productivity at station KNOT
48 (44N, 155E) in the sub-arctic western North Pacific. *Deep Sea Research Part II: Topical Studies in Oceanography*, 49, 5395-
49 5408. doi: 10.1016/S0967-0645(02)00198-4, 2002.

50 Kaupp, L. J., Measures, C. I., Selph, K. E., & Mackenzie, F. T.: The distribution of dissolved Fe and Al in the upper waters of
51 the Eastern Equatorial Pacific. *Deep Sea Research Part II: Topical Studies in Oceanography*, 58(3-4), 296-310, 2011

52 Ishizaki, H.: A simulation of the abyssal circulation in the North Pacific Ocean. Part II: Theoretical rationale. *Journal of*
53 *physical oceanography*, 24(9), 1941-1954, 1994

54 Koch, F., Marcoval, A., Panzeca, C., Bruland, K. W., et al.: The effects of vitamin B12 on phytoplankton growth and
55 community structure in the Gulf of Alaska. *Limnology and Oceanography*, 3, 1023–1034. doi: 10.4319/lo.2011.56.3.1023,
56 2011.

57 Kohonen, T.: Self-organized formation of topologically correct feature maps. *Biol. Cybern.* 43, 59-69.
58 doi:10.1007/BF00337288, 1982.

59 Kumar N., Anderson R.F., Mortlock R.A., Froelich P.N.: Increased biological productivity and export production in the glacial
60 Southern-Ocean. *Nature*. 378, 675–680. doi: 10.1038/378675a0, 1995

61 Kuragano, T., & Kamachi, M.: Balance of volume transports between horizontal circulation and meridional overturn in the
62 North Pacific subarctic region. *Journal of oceanography*, 60, 439-451, 2004

63 Landry M.R., Selph K.E., Taylor A.G., Décima M., et al.: Phytoplankton growth, grazing and production balances in the
64 HNLC equatorial Pacific. *Deep-sea Res. II*. 58, 524-535. doi: 10.1016/j.dsr2.2010.08.011, 2011.

65 Lauderdale, J.M., Braakman, R., Dutkiewicz, S., Follows, M.J.: Microbial feedbacks optimize ocean iron availability.
66 *Proceedings of the National Academy of Sciences*, 117(9), 4842-4849. doi: 10.1073/pnas.1917277117, 2020.

67 Liu, Y., R.H., Weisberg, S. Vignudelli, and G.T. Mitchum.: Patterns of the Loop Current system and regions of sea surface
68 height variability in the eastern Gulf of Mexico revealed by the self-organizing maps, *Journal of Geophysical Research*
69 *Oceans*, 121, 2347-2366, <http://dx.doi.org/10.1002/2015JC011493>, 2016

70 Lumpkin, R., & Speer, K.: Global ocean meridional overturning. *Journal of Physical Oceanography*, 37(10), 2550-2562, 2007

71 Maritorena, S., & Siegel, D. A.: Consistent merging of satellite ocean color data sets using a bio-optical model. *Remote Sensing*
72 *of Environment*, 94(4), 429-440, 2005

73 Marrari, M., Piola, A.R., Valla, D.: Variability and 20-Year Trends in Satellite-Derived Surface Chlorophyll Concentrations
74 in Large Marine Ecosystems around South and Western Central America. *Frontiers in Marine Science*, 21 doi:
75 10.3389/fmars.2017.00372, 2017.

76 Martin, J.H., Fitzwater, S.E.: Iron deficiency limits phytoplankton growth in the northeast Pacific subarctic. *Nature*. 331, 341–
77 343. doi: 10.1038/331341a0, 1988.

78 Martin, J.H.: Glacial-interglacial CO₂ change: the iron hypothesis. *Paleoceanography*. 5, 1-13. doi:
79 10.1029/PA005i001p00001, 1990.

80 Martin, J.H., Fitzwater, S.E., Gordon, R.M.: Iron deficiency limits phytoplankton growth in Antarctic waters. *Global*
81 *Biogeochemical Cycles*, 4, 5-12. doi:10.1029/GB004i001p00005, 1990.

82 Martin, J.H., Coale, K.S., Johnson, K.S., Fitzwater, S.E. et al.: Testing the iron hypothesis in ecosystems of the equatorial
83 Pacific Ocean. *Nature*. 371, 123–129. doi:10.1038/371123a0, 1994.

84 Martínez-García A., Rosell-Melé A., Geibert W., Gersonde R., et al.: Links between iron supply, marine R. productivity, sea
85 surface temperature, and CO₂ over the last 1.1 Ma. *Paleoceanography*. 24, PA1207. doi: 10.1029/2008PA001657, 2009

86 McPhaden, M.J.: Trade wind fetch related variations in Equatorial Undercurrent depth, speed, and transport. *Journal of*
87 *Geophysical Research: Oceans*, 98(C2), 2555–2559. doi: 10.1029/92JC02683, 1993.

88 McPhaden, M. J., & Zhang, D.: Slowdown of the meridional overturning circulation in the upper Pacific Ocean. *Nature*,
89 415(6872), 603-608, 2002

90 Mélin, F., Vantrepotte, V., Chuprin, A., Grant, M., Jackson, T., & Sathyendranath, S.: Assessing the fitness-for-purpose of
91 satellite multi-mission ocean color climate data records: A protocol applied to OC-CCI chlorophyll-a data. *Remote Sensing of*
92 *Environment*, 203, 139-151, 2017

93 Minas, H. J., Minas, M., Packard, T.T.: Productivity in upwelling areas deduced from hydrographic and chemical fields.
94 *Limnology and Oceanography*. 31, 1182-1206. doi: 10.4319/lo.1986.31.6.1182, 1986.

95 Moat B.I.; Frajka-Williams E., Smeed D.A.; Rayner D.; Johns W.E.; Baringer M.O.; Volkov, D.; Collins, J.: Atlantic
96 meridional overturning circulation observed by the RAPID-MOCHA-WBTS (RAPID-Meridional Overturning Circulation and
97 Heatflux Array-Western Boundary Time Series) array at 26N from 2004 to 2020. British Oceanographic Data Centre - Natural
98 Environment Research Council, UK. doi:10.5285/e91b10af-6f0a-7fa7-e053-6c86abc05a09, 2022

99 Moat, B. I., Smeed, D. A., Frajka-Williams, E., Desbruyères, D. G., Beaulieu, C., Johns, W. E., ... & Bryden, H. L.: Pending
00 recovery in the strength of the meridional overturning circulation at 26 N. *Ocean Science*, 16(4), 863-874, 2020

01 Moore, J.K., Doney, S.C., 2007. Iron availability limits the ocean nitrogen inventory stabilizing feedbacks between marine
02 denitrification and nitrogen fixation. *Global Biogeochemical Cycles*, 21, GB2001. doi:10.1029/2006GB002762, 2013

03 Moore, C.M., Mills, M.M., Arrigo, K.R., Berman-Frank, I., et al.: Processes and patterns of oceanic nutrient limitation. *Nature*
04 *Geoscience*, 6, 701–710. doi: 10.1038/ngeo1765 , 2013

05 Moore, J.K., Fu, W., Primeau, F., Britten, G.L. et al.: Sustained climate warming drives declining marine biological
06 productivity. *Science*, 359 (6380), 1139-1143. doi:10.1126/science.aao6379, 2018.

07 Moradi, M.: Evaluation of merged multi-sensor ocean-color chlorophyll products in the Northern Persian Gulf. *Continental*
08 *Shelf Research*, 221, 104415, 2021

09 Muglia, J., Skinner, L. C., & Schmittner, A.: Weak overturning circulation and high Southern Ocean nutrient utilization
10 maximized glacial ocean carbon. *Earth and Planetary Science Letters*, 496, 47-56, 2018

11 Nielsdóttir, M.C., Moore, C.M., Sanders, R., Hinz D.J. et al.: Iron limitation of the postbloom phytoplankton communities in
12 the Iceland Basin, *Global Biogeochemical Cycles*, 23, GB3001, doi:10.1029/2008GB003410, 2009.

13 Nishioka, J., Obata, H., Ogawa H., Ono, K., et al.: Sub-polar marginal seas fuel the North Pacific through the intermediate
14 water at the termination of the global ocean circulation. *Proc. Natl. Acad. Sci.*, 117 (23), pp. 12665-
15 12673, 10.1073/pnas.2000658117, 2020

16 Nishioka, J., et al.: Iron supply to the western subarctic Pacific: Importance of iron export from the Sea of Okhotsk. *J. Geophys.*
17 *Res.*, 112, C10012, doi:10.1029/2006JC004055, 2007

18 Ono, T., Shiomoto, A., Saino T.: Recent decrease of summer nutrients concentrations and future possible shrinkage of the
19 subarctic North Pacific high-nutrient low-chlorophyll region. *Global Biogeochemical Cycles*, 22, GB3027.
20 doi:10.1029/2007GB003092, 2008.

21 Oliver, M. J., & Irwin, A. J.: Objective global ocean biogeographic provinces. *Geophysical research letters*, 35(15), 2018

22 Orsi, A. H., Whitworth, T., and Nowlin, W. D.: On the meridional extent and fronts of the Antarctic Circumpolar Current.
23 *Deep Sea Res. I Oceanogr. Res. Papers* 42, 641–673. doi: 10.1016/0967-0637(95)00021-W, 1995

24 Parekh, P., Follows, M.J., Boyle, E.A.: Decoupling of iron and phosphate in the global ocean. *Global Biogeochemical Cycles*,
25 19, GB2020, doi:10.1029/2004GB002280, 2005.

26 Pitchford, J.W., Brintley, J.: Iron limitation, grazing pressure and oceanic high nutrient-low chlorophyll (HNLC) regions.
27 *Journal of Plankton Research*, 21, 525-547. doi: 10.1093/plankt/21.3.525, 1999.

28 Polovina, J.J., Howell, E.A., Abecassis, M.: Ocean's least productive waters are expanding. *Geophysical Research Letters*, 35.
29 doi: 10.1029/2007GL031745, 2008.

30 Qiu B.: Large-scale variability in the midlatitude subtropical and subpolar North Pacific Ocean: Observations and causes.
31 *Journal of Physical Oceanography*, 32, 353–375. doi: 10.1175/1520-0485(2002)032<0353:LSVITM>2.0.CO;2, 2002

32 Racault, M.F., Sathyendranath, S., Brewin, R. J. W., Raitso, et al.: Impact of El Niño variability on oceanic phytoplankton.
33 *Frontiers in Marine Science*, 4, 133. doi: 10.3389/fmars.2017.00133, 2017.

34 Radenac, M.-H., Léger, F., Singh, A., Delcroix, T.: Sea surface chlorophyll signature in the tropical Pacific during eastern and
35 central Pacific ENSO events. *Journal of Geophysical Research: Oceans*, 117, C04007. doi: 10.1029/2011JC007841, 2012.

36 Riebesell, U., Körtzinger, A., Oschlies, A.: Sensitivities of marine carbon fluxes to ocean change. *Proc. Natl. Acad. Sci. USA*.
37 doi: 10.1073/pnas.0813291106, 2009

38 Serno, S., Winckler G., Anderson, R.F., Hayes, C T. et al.: Eolian dust input to the Subarctic North Pacific. *Earth and Planetary
39 Science Letters*. 387, 252-263. doi:10.1016/j.epsl.2013.11.008, 2014

40 Sen, P.K.: Estimates of the regression coefficient based on Kendall's Tau Pranab Kumar Sen. *Journal of the American
41 Statistical Association*. 63, 1379–1389, 1968

42 Schmidt, K., Schlosser, C., Atkinson, A., Fielding, S., Venables, H. J., Waluda, C. M., & Achterberg, E. P.: Zooplankton gut
43 passage mobilizes lithogenic iron for ocean productivity. *Current Biology*, 26(19), 2667-2673, 2016

44 Schmittner, A.: Decline of the marine ecosystem caused by a reduction in the Atlantic overturning circulation. *Nature*.
45 434(7033), 628-33. doi: 10.1038/nature03476, 2005.

46 Schneider, N., Miller, A. J., Alexander, M. A., & Deser, C.: Subduction of decadal North Pacific temperature anomalies:
47 Observations and dynamics. *Journal of Physical Oceanography*, 29(5), 1056-1070, 1999

48 Smeed, D. A., Josey, S. A., Beaulieu, C., Johns, W. E., Moat, B. I., Frajka-Williams, E., et al.: The North Atlantic Ocean is in a
49 state of reduced overturning. *Geophysical Research Letters*, 45, 1527–1533. <https://doi.org/10.1002/2017GL076350>, 2018

50 Smeed, D. A., Moat, B., Rayner, D., Johns, W.E. et al.: Atlantic meridional overturning circulation observed by the RAPID-
51 MOCHA-WBTS (RAPID-Meridional Overturning Circulation and Heatflux Array-Western Boundary Time Series) array at
52 26N from 2004 to 2018. British Oceanographic Data Centre - Natural Environment Research Council, UK. doi:
53 10.5285/8cd7e7bb-9a20-05d8-e053-6c86abc012c2, 2019.

54 Tagliabue, A., Aumont, O., Bopp, L.: The impact of different external sources of iron on the global carbon cycle. *Geophysical
55 Research Letters*, 41, 920–926. doi: 10.1002/2013GL059059, 2014.

56 Takeda, S.: Iron and phytoplankton growth in the Subarctic North Pacific. *Aqua-BioScience Monographs*, 4, 41–93, 2011.

57 Tandon, N. F., Saenko, O. A., Cane, M. A., & Kushner, P. J.: Interannual variability of the global meridional overturning
58 circulation dominated by Pacific variability. *Journal of Physical Oceanography*, 50(3), 559-574, 2020

59 Timmermann, A., Okumura, Y., An, S. I., Clement, A., Dong, B., Guilyardi, E., et al.: The influence of a weakening of the
60 Atlantic meridional overturning circulation on ENSO. *Journal of climate*, 20(19), 4899-4919, 2007

61 Torrence, C., Compo, G.: A practical guide to wavelet analysis. *Bulletin of the American Meteorological society*, 79, 61–78.
62 doi: 10.1175/1520-0477, 1998.

63 Torrence, C., Webster, P.J.: Interdecadal changes in the ENSO-monsoon system. *Journal of Climate*, 12, 2679-2710. doi:
64 10.1175/1520-0442, 1999.

65 Tsuda, A., Takeda S., Saito H., Nishioka J., et al.: A mesoscale iron enrichment in the western subarctic Pacific induces a large
66 centric diatom bloom. *Science*. 300, 958– 961. doi:10.1126/science.1082000, 2003.

67 Tyrrell, T., Merico, A., Waniek, J.J., Wong, et al.: Effect of seafloor depth on phytoplankton blooms in high-nitrate, low-
68 chlorophyll (HNLC) regions. *Journal of Geophysical Research: Biogeosciences*, 110, G02007, doi: 10.1029/2005JG000041,
69 2005.

70 Vatanen, T., Osmala, M., Raiko, T., Lagus, K. et al.: Self-organization and missing values in SOM and GTM. *Neurocomputing*.
71 147, 60–70. doi: 10.1016/j.neucom.2014.02.061, 2015.

72 Vesanto, J., Himberg, J., Alhoniemi, E., Parhankangas, J.: Self-organizing map in Matlab: the SOM Toolbox. In: *Proceedings*
73 *of the Matlab DSP conference*, Espoo, Finland, Comsol Oy, 1999.

74 Warren, B. A.: Why is no deep water formed in the North Pacific?. *Journal of Marine Research*, 41(2), 327-347, 1983

75 Winckler, G., Anderson, R.F., Jaccard, S.L., Marcantonio, F.: Ocean dynamics, not dust, have controlled equatorial Pacific
76 productivity over the past 500,000 years. *Proceedings of the National Academy of Sciences*, 113, 6119–6124.
77 doi:10.1073/pnas.1600616113, 2016.

78 Yaremchuk, M., Bindoff, N. L., Schröter, J., Nechaev, D., & Rintoul, S. R.: On the zonal and meridional circulation and ocean
79 transports between Tasmania and Antarctica. *Journal of Geophysical Research: Oceans*, 106(C2), 2795-2814, 2001

80 Yasunaka, S., Nojiri, Y., Nakaoka, S., Ono, T. et al.: Mapping of sea surface nutrients in the North Pacific: Basin-wide
81 distribution and seasonal to interannual variability. *journal of geophysical research: oceans*, 119, 7756–7771. doi:
82 10.1002/2014JC010318, 2014.

83 Yasunaka, S., Ono, T., Nojiri, Y., Whitney, F.A., et al.: Long-term variability of surface nutrient concentrations in the North
84 Pacific, *Geophysical Research Letters*, 43, 3389-3397. doi:10.1002/2016GL068097, 2016.

85
86

87

88 **Tables**

89

90 Table 1. Mean±std characteristics of each of the SOM-defined HNLC subregions (R1 to R5). NO₃ (mmol
 91 m⁻³) and Chl (mg m⁻³) values are respectively from model and satellite data. Decadal chlorophyll trends
 92 (ΔChl, mgChl m⁻³ decade⁻¹) are calculated from the mean time-series of monthly deseasonalized
 93 chlorophyll.

94

| Region | Subregion | NO ₃ (μM) | Chl (mg m ⁻³) | NO ₃ :Chl (mmol NO ₃ mg Chl ⁻¹) | ΔChl (mg m ³ decade ⁻¹) |
|--------|-----------|-------------------------|------------------------------|--|---|
| SNP | R1 | 4.51 ± 1.02 | 0.31 ± 0.07 | 15 ± 3 | +0.05 |
| | R2 | 8.05 ± 0.88 | 0.36 ± 0.07 | 23 ± 6 | +0.26 |
| | R3 | 15.52 ± 2.27 | 0.49 ± 0.16 | 35 ± 15 | +0.43 |
| EEP | R1 | 4.04 ± 0.77 | 0.22 ± 0.02 | 18 ± 3 | +0.01 |
| | R2 | 6.63 ± 1.42 | 0.39 ± 0.05 | 20 ± 4 | +0.08 |
| SO | R1 | 4.13 ± 1.05 | 0.22 ± 0.06 | 20 ± 4 | +0.24 |
| | R2 | 9.11 ± 1.23 | 0.31 ± 0.06 | 31 ± 9 | +0.42 |
| | R3 | 15.73 ± 1.07 | 0.32 ± 0.10 | 55 ± 17 | +0.47 |
| | R4 | 23.26 ± 1.06 | 0.26 ± 0.16 | 104 ± 32 | +0.62 |
| | R5 | 29.18 ± 1.57 | 0.43 ± 0.92 | 103 ± 54 | +0.46 |

95

96

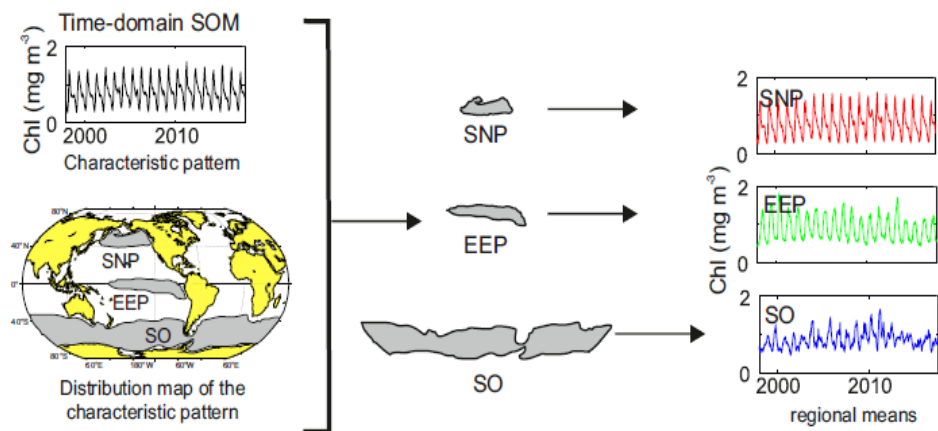
97 Table 2. Basic statistics of the extent of each of the SOM-defined HNLC subregions during the
 98 analyzed period (1998-2017).

99

| Region | Mean extent±S.D. (x10 ⁶ km ²) | % of total extent | Min-Max (x10 ⁶ km ²) | Max. Variation (x10 ⁶ km ²) | C.V.% |
|--------|---|----------------------|--|---|-------|
| SNP | 7.7±3.6 | 8.4 | 3.8-15.9 | 12.1 | 47 |
| EEP | 7.8±0.4 | 8.4 | 7.3-8.4 | 1.1 | 5 |
| SO | 76.5±0.9 | 83.2 | 61.3-86.8 | 25.5 | 12 |

00

01

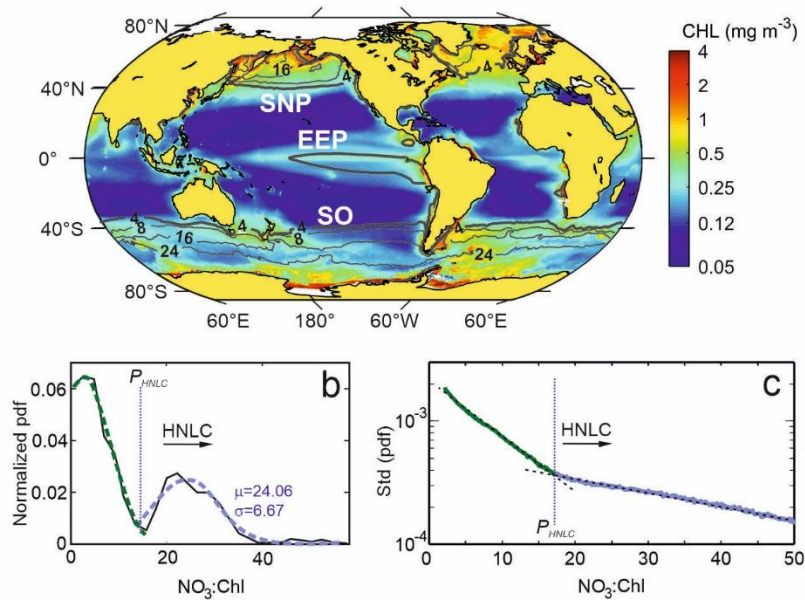


03

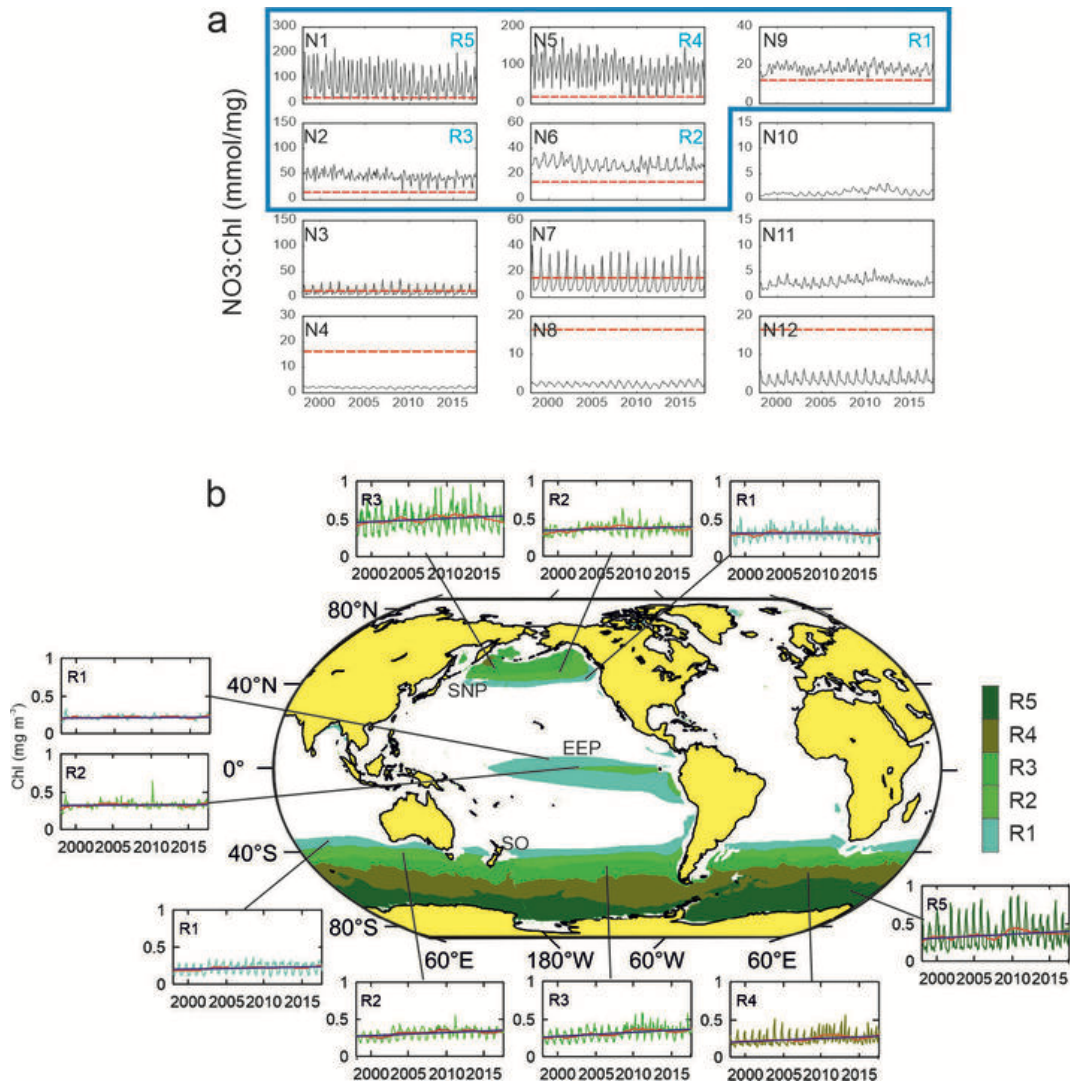
04 Figure 1. Scheme of a characteristic pattern and its distribution map obtained from SOM time-domain
 05 analysis at global and regional means calculated for each of the HNLC regions.

06

07



10 Figure 2. a) Global mean satellite Chl concentrations (mg m^{-3}) for the period 1998-2018 and superimposed
 11 surface NO_3 contour lines (from modeling data (isolines are drawn at 4 mmol m^{-3} intervals). b)
 12 Normalized probability density function of the values of the $\text{NO}_3:\text{Chl}$ ratio obtained from the SOM
 13 temporal patterns. Green and blue lines show the fit to a normal distribution for the first and second pdf
 14 modes, respectively. c) Standard deviation of the probability density function (*pdf*) of the $\text{NO}_3:\text{Chl}$
 15 (mmol/mg) monthly ratios obtained for the 20 years analyzed. Note that the y-axis scale is logarithmic.
 16 The critical point ratio $P_{\text{HNLC}} = 17 \text{ mmolNO}_3 \text{ mgChl}^{-1}$ delimits HNLC regions from macronutrient limited
 17 regions.

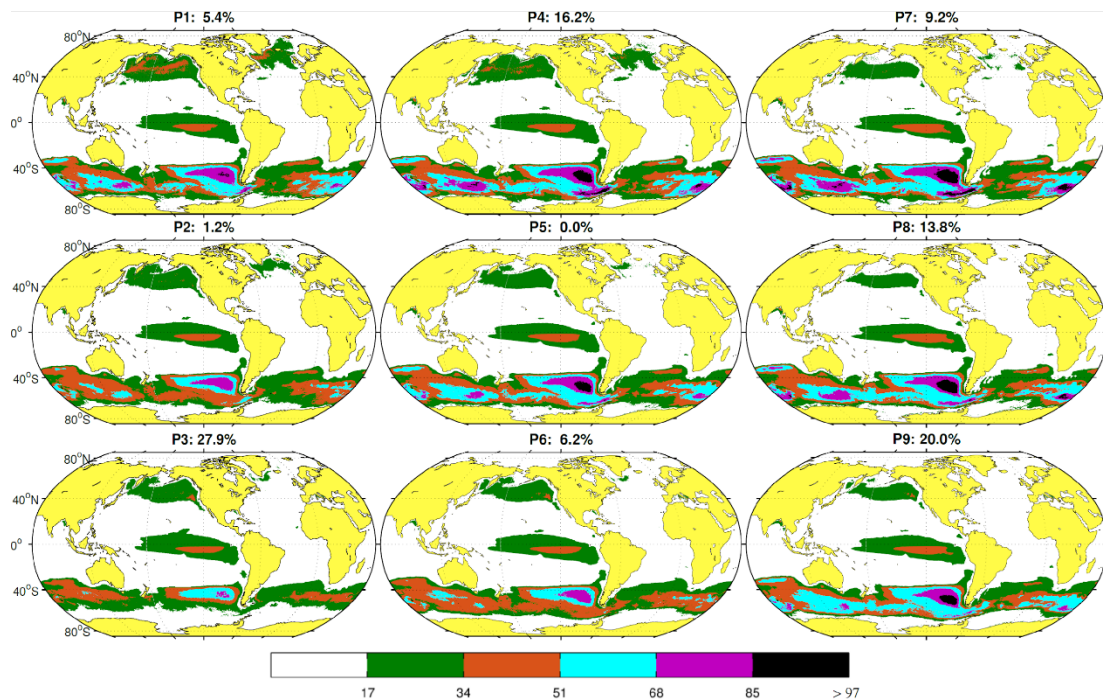


20

21

22 Figure 3. a) Characteristic temporal variability patterns of NO₃:Chl ratios (N1-N12) as unveiled by the
 23 4x3 SOM analysis in the time domain. Red dashed lines indicate the P_{HNLC} value b) Coherent regions of
 24 HNLC variability (SNP, EEP, and SO) and corresponding subregions (R1 to R5) associated with the
 25 SOM temporal patterns exhibiting only NO₃:Chl values larger than P_{HNLC} all the times throughout the
 26 entire analyzed period (i.e. identified with N9, N6, N2, N5 and N1) . Patterns corresponding to a subregion
 27 in the northern and southern hemispheres present a similar pattern although seasonally lagged (6-month
 28 delay). Insets show the time series of the averaged Chl over the corresponding subregion (complete map
 29 of regions of NO₃:Chl variability and corresponding temporal variability patterns are shown in Fig. S1).
 30 The red line represents the 24-month filtered series and the blue line indicates the trend (values shown in
 31 Table 1).

32



33

34 Figure 4. Characteristic spatial patterns (P1 to P9) of HNLC regions as defined by $\text{NO}_3:\text{Chl}$ ratios $>$
35 P_{HNLC} . The value on top of each pattern indicates its probability of occurrence over the 20-year period
36 analyzed. To preserve the topology, the SOM algorithm introduces some patterns with zero probability
37 of occurrence, such as P5. The colorbar indicates the different $\text{NO}_3:\text{Chl}$ ranges represented.

38

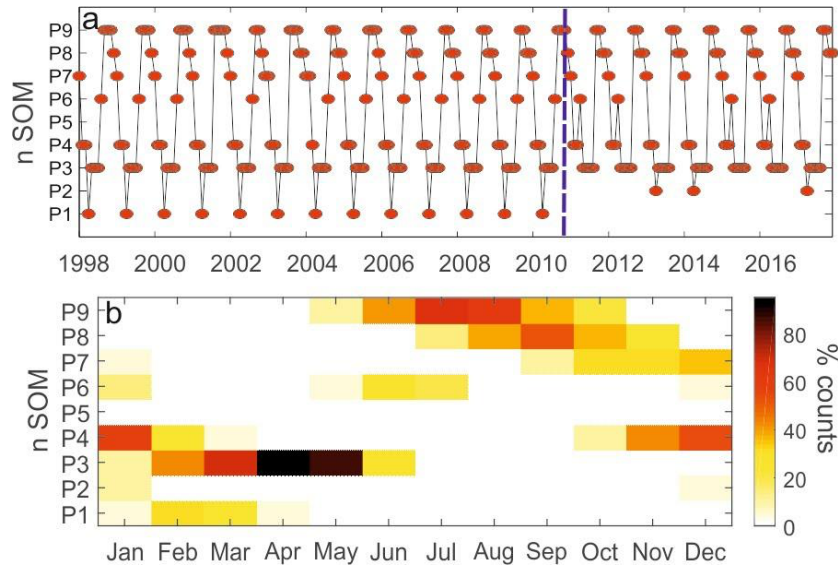
39

40

41

42

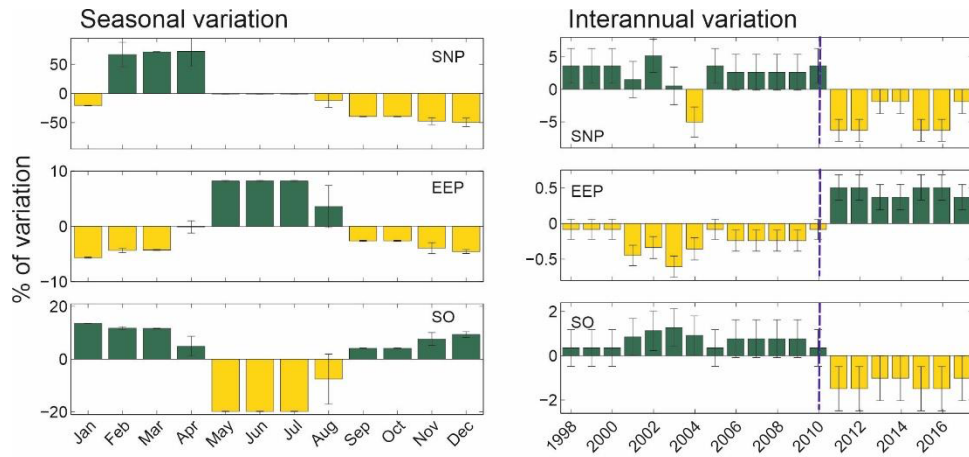
43



44

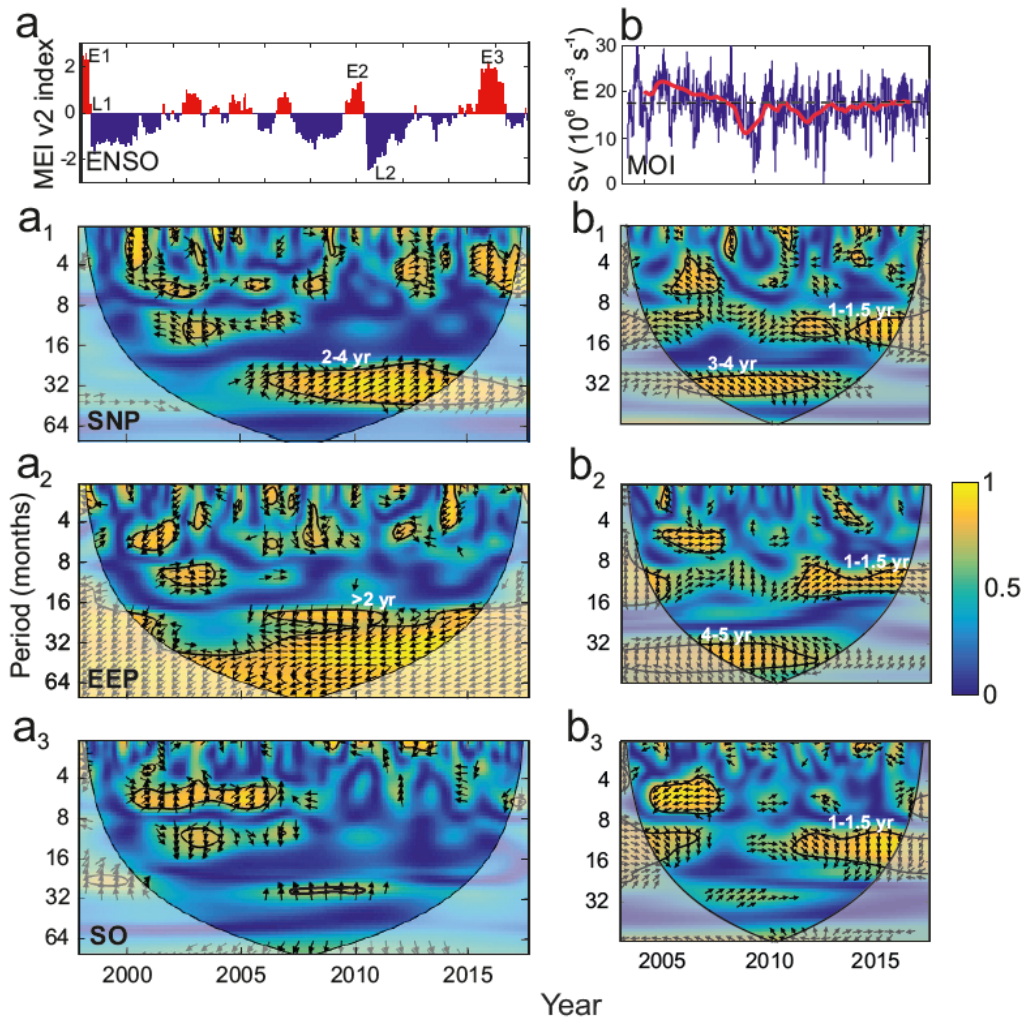
45

46 Figure 5. a) Time evolution of the spatial patterns as defined by the Best Matching Units (BMUs) for the
 47 period of 1998-2018. The blue dashed line indicates the regime shift occurring after 2010. b) Monthly
 48 frequency of occurrence of the spatial patterns identified in Figure 4.



49

50 Figure 6. Seasonal (left) and interannual variations (right) in the spatial extent of the three HNLC regions,
 51 represented as a percentage of variation from the mean extent of each region. Variations are referred to
 52 the mean extension of each region. Dark and light-colored bars indicated positive and negative values,
 53 respectively. The blue dashed lines indicate the regime shift occurring after 2010.
 54
 55



56

57 Figure 7. a) ENSO (MEI v2) index. E1-E3 indicate intense El Niño episodes and L1 and L2 mark strong
 58 La Niña periods. a1, a2, a3 display the cross-wavelet coherence between NO₃:Chl ratio and ENSO for
 59 each of the HNLC regions. b) Meridional overturning (AMOC) volume transport for the period (2004-
 60 2017) measured at 26.5°N (Smeed et al., 2016). The red line shows interannual component is obtained by
 61 filtering the data with a 540-day low-pass filter after the removal of the mean seasonal cycle. b₁, b₂, and
 62 b₃ display the cross-wavelet coherence between NO₃:Chl ratio and AMOC for each of the HNLC regions.
 63 The thick black contours in the cross-wavelet coherence figures designate the 95% confidence levels and the
 64 cone of influence where edge effects are not negligible is shown as a lighter shade. The arrows indicate
 65 the phase relationship between the signals with the horizontal component indicating in-phase (rightward)
 66 or out-of-phase (leftward) and the vertical component indicating a 90° phase difference lagging (upward)
 67 or leading (downward). Period units are months.

68